CLM-R235

CLM-R235

UKAEA

Report

THE BUNDLE DIVERTOR

A REVIEW OF EXPERIMENTAL RESULTS

K. B. Axon
J. Burt
S. K. Erents
S. J. Fielding
R. D. Gill
D. H. J. Goodall
M. Hobby
J. Hugill
G. M. McCracken
J. W. M. Paul
N. J. Peacock
B. A. Powell
R. Prentice
G. Proudfoot
G. W. Reid
A. D. Sanderson
P. E. Stott
D. D. R. Summers
C. M. Wilson
A. J. Wootton

CULHAM LABORATORY
Abingdon Oxfordshire

1983

C/18

Available from H. M. Stationery Office

£4.00

CLM-R235

THE BUNDLE DIVERTOR
A REVIEW OF EXPERIMENTAL RESULTS

K.B. Axon, J. Burt, S.K. Erents, S.J. Fielding, R.D. Gill*
D.H.J. Goodall, M. Hobby, J. Hugill, G.M. McCracken, J.W.M. Paul,
N.J. Peacock, B.A. Powell, R. Prentice*, G. Proudfoot, G.W. Reid,
A.D. Sanderson†, P.E. Stott*, D.D.R. Summers*, C.M. Wilson, A.J. Wootton□

Culham Laboratory, Abingdon, Oxon., OX14 3DB, UK
(Euratom/UKAEA Fusion Association)

*JET Joint Undertaking, Abingdon, Oxon., OX14 3DB, UK

†Oxford University, Oxon., UK

□Oak Ridge National Laboratory, Thermonuclear Division,
PO Box Y, Oak Ridge, Tennessee 37830, USA.

October 1982

ISBN 0 85311 120 0

THE BUNDLE DIVERTOR

PART III : EXPERIMENTAL RESULTS

ABSTRACT

This paper is a review of the experimental results obtained with a tokamak, DITE, operated with a bundle divertor. Experiments to determine the magnetic aperture, exhaust and screening properties of the divertor are described. The results are compared with the predictions of various models. A comparison of the plasma parameters produced with and without the divertor is presented. The differences are discussed in terms of the exhaust and screening properties, with the aid of a global model of impurity production. Neutral hydrogen atom injection has been used to heat the plasma; results are presented, together with a discussion of the effect of the magnetic field ripple, produced by the divertor, on confinement. Gross instability characteristics of plasma produced with the divertor are discussed, together with their effect on the divertor properties. Possible explanations for different operational characteristics are considered. Finally, a comparison between the results obtained with the bundle divertor, and poloidal divertors, is presented.

CONTENTS

1 INTRODUCTION

The bundle divertor [1,2,3] is a device whose purpose is to improve the plasma purity by reducing the interaction between the plasma and the torus walls and limiters. It also provides a means of exhausting plasma from the main torus. Two coils distort the toroidal magnetic field and divert field lines from the outer layer of the plasma into a separate divertor chamber where they intersect a target. In this way the main plasma surface interaction is removed from the torus as shown in Figure 1. A description of the magnetic field configuration and consequent predicted plasma behaviour, has been published [2,3]. A large amount of experimental data has been obtained from DITE bundle divertor experiments [4-19]. This paper attempts to coherently combine these earlier results with the later ones and thus present a summary of all the experimental work.

DITE is the first and only tokamak to have a bundle divertor.

The main properties of the divertor, which will be described are:

a) Magnetic limiter. The divertor produces a magnetic separatrix, minor radius, a_s, outside which field lines are diverted. Figure 1 illustrates the geometry. The separatrix controls the plasma volume without introducing a material limiter.

b) Plasma exhaust. Charged particles diffusing across the separatrix can flow along the diverted field lines into the divertor chamber, where they are neutralised on a target plate, and pumped away. The particles which are diverted transport energy, and cool the plasma edge. These two effects reduce the plasma-limiter interaction, and diminish the impurity influx.

c) Plasma screening, or shielding. Impurities originating from the

limiters and vacuum vessel walls may be ionised in the scrape-off layer outside the separatrix ($a_s < r < a_L$), and swept into the divertor before penetrating the main plasma. In this way the plasma is screened, or shielded, from the incoming flux.

Each of the above functions has been successfully demonstrated on DITE.

The first section of this paper describes the tokamak and divertor, summarising the magnetic field configuration. Two divertors have been used, the MkIA (from 1976 to 1977) being replaced by the MkIB (from February 1979 to June 1980) after a coil failure. Throughout this paper the emphasis is on the later results, with comparisons drawn, where suitable, with the early results. A separate section is devoted to the difference observed in the operational behaviour of the two divertors, and possible causes.

The magnetic limiter effect is described in terms of the operating regime in plasma current and density space for the tokamak. This is followed by a description of experiments directed at measuring the particle and energy exhaust, impurity screening, and particle retention in the divertor target chamber. It is these properties which combine to reduce the impurity content of the plasma. Because of the difficulty experienced in obtaining stable discharges with a wide range of plasma current, most of the scaling of parameters is with plasma density. The results are compared with the predictions of various theoretical models.

A comparison between plasma produced with and without the divertor is presented, with emphasis on the different impurity behaviour. A global model, describing the behaviour of both the working gas and impurities, is developed in order to understand the experimental

results in terms of the measured exhaust and screening coefficients.

Neutral beam injection has been used to double the ion temperature, and results are presented. Some comments are included on the importance of the perturbed magnetic field within the main plasma. A section is also devoted to the gross instability behaviour observed when the divertor is operated. The effect of the instabilities on the divertor operation is discussed. Except for this section, all results presented were obtained with grossly stable plasmas.

After this detailed description of the results obtained predominantly with the MkIB divertor, the differences in plasma behaviour obtained with the MkIA and MkIB are discussed. It is emphasised that the MkIA results were exploratory, and the importance of maintaining a constant density, and the role of instabilities and suprathermal electrons, have only been understood from the later experiments.

A final section deals with the comparison of the results presented here, and those obtained with other types of divertors. Improvements in bundle divertor design are considered.

2 THE TOKAMAK AND DIVERTOR

Details of DITE tokamak are given in references [5] and [21]. Table 1 lists typical parameters of the tokamak and divertor, together with some characteristic plasma conditions. Figure 2 is a plan of the machine, showing the relative positions of the divertor, injectors, and relevant diagnostics. Without the divertor, toroidal fields $B_\phi \lesssim 2.7$T and plasma currents $I_p \lesssim 250$kA are used. When operating with the divertor, electro-mechanical and thermal stresses restrict $B_\phi \lesssim 1.5$T. The majority of results were obtained with $B_\phi \simeq 1$T, but a short period of operation with $B_\phi \simeq 1.5$T was undertaken with the MkIB.

Table I summarises the different operating conditions. Whereas the MkIA was operated with hydrogen working gas, molybdenum limiters (a_L = 0.27m), and a separatrix radius a_s = 0.16m, the MkIB was operated predominantly with deuterium, titanium limiters (a_L = 0.26m) and a_s = 0.175m. [In some publications, the incorrect value a_s = 0.19m was quoted for the MkIA.] The increase in the separatrix minor radius allowed routine operation with the MkIB at ~ 30% higher plasma currents and densities.

The magnetic geometry has been previously described in detail [2], and is briefly summarised here.

Two parameters which characterise the magnetic configuration are the divertor acceptance angle, $2\pi/q_D$, and the mirror ratio, M [2,3]. q_D is the number of revolutions of the torus a field line in the scrape-off layer makes before it enters the divertor. This varies from infinity at the separatrix to ~ 4 at the limiter, with a spatial dependence $q_D \propto (r - a_s)^{-\frac{1}{2}}$. Computed average values, $\bar{q}_D$ are ~ 7. This means that 1/7 of the flux in the annulus between a_s and a_L will be diverted on the next transit around the machine, in each direction. The boundary between field lines which will be diverted, and those which will by-pass the divertor on the next transit of the torus, is shown in Figure 3 in the unperturbed radial plane, 180° in major azimuthal angle from the divertor. Field lines passing through the shaded areas, bounded by the separatrix and the limiter, will be diverted on the next transit of the torus, following in one case a clockwise and in the other case an anti-clockwise direction.

The mirror ratio quoted in Table 1, M ≃ 4, is the computed ratio of the maximum field (at the plane of a divertor coil) to the toroidal

field at the vacuum vessel centre. The magnetic field reduces again as a field line is followed from the plane of a divertor coil towards the target plate.

Typical plasma current durations are 0.2 to 0.5s. The divertor coil current rises to a maximum value in about 0.15s and is maintained at this value for about 0.2s. The machine is usually operated so that the divertor current reaches its maximum value as the plasma current is initiated. Alternative modes of operation consist of switching the divertor on during the discharge, either by delaying the divertor current, or initially displacing the plasma to a reduced major radius and then returning it to the centre of the torus. Because the toroidal and divertor fields specify a fixed stagnation axis, the separatrix major radius, but not minor radius, is fixed. Moving the plasma inwards by more than 85mm (MkIB) ensures that the outer flux surface is defined by the limiters and not the separatrix.

The divertor target consists of two metal sheets, with dimensions 280mm by 140mm by (0.5 to 5)mm. Stainless steel, titanium and molybdenum have been used. Figure 4 shows a target plate which has been damaged by low density discharges. The damage contours correspond to the computed magnetic field line intersections with the plate.

The target plates are usually electrically connected to the target chamber and torus walls. Between each discharge titanium is deposited on the target chamber walls to inhibit particle induced desorption, and to pump neutral gas. Pumping speeds at the target up to 5×10^4 ℓs^{-1} are estimated, which would allow about 15% of untrapped particles to return to the torus.

3 THE MAGNETIC LIMITER

The toroidal and divertor fields cancel to produce a stagnation axis where $B_\phi = 0$ [see Figures 1 and 3]. Magnetic field lines through the stagnation axis behave as separatrix field lines; the separatrix field line with the smallest minor radius defines a toroidal boundary of minor radius a_s, the separatrix radius. The rotational transform generated by the poloidal and toroidal fields ensures that all field lines with a radius $r > a_s$ will eventually pass through the divertor.

The separatrix plays the role of a magnetic limiter. Its position is computed by following field lines produced by superimposing the divertor coil fields on those of an axisymmetric plasma equilibrium configuration. Experimentally, its location is verified by electron beam trajectories in the toroidal and divertor fields, and by moving a limiter into the plasma until no interaction between plasma and target plate is observed. The computed and measured location agree to within 5mm.

The plasma current-carrying volume is determined by the separatrix. This is first demonstrated by plotting the operating regime [21,22], ie, that region in $(1/q_L, \bar{n}_{eL}/B_\phi)$ space where stable discharges can be obtained for discharges with and without the divertor. Here q_L is the safety factor at the limiter, $2\pi a_L^2 B_\phi/(\mu_o I_p R)$, and $\bar{n}_{eL}$ is the line of sight average density, $(\int_o^{a_L} n_e \, dr)/a_L$. Figure 5a shows that without the divertor, $q_L \gtrsim 2$, and the operating region is restricted by plasma current disruptions. With the divertor, $q_L > 4.5$ for stability. Discharges with $q_L < 4.5$ can be achieved but the resulting plasmas are very unstable (see Section 11). The divertor restricts the maximum current and density which can be obtained. An alternative representation is shown in Figure 5b where, with the divertor on, the values at

the separatrix, $1/q_s$ and $\bar{n}_{es}$, are plotted. These are evaluated assuming no current or particles outside the separatrix. This second normalisation produces better agreement than the first between divertor on and off, suggesting that the separatrix plays the role of a limiter in determining the plasma size. The discrepancy still present between the two cases can be explained if about 10% of the current flows outside the separatrix. Whereas titanium gettering of the vacuum vessel with no divertor allows a larger region in $(1/q, \bar{n}_e/B_\phi)$ space to be accessed, results obtained with the divertor show little difference.

Operation with the divertor, but without the target plate, allows only a small increase ($\sim$ 20%) in the values of $1/q_L$ and $\bar{n}_{eL}$. From Figure 3 it can be seen that only the flux lines in the cross hatched region which is common to the divertor bundles on both sides of the plate return to the scrape off layer. The remainder either hit the wall of the divertor chamber (after passing through the plane where the target plate would be) or return to the torus outside the limiter radius. As this is seen to be only a small part of the divertor flux bundle, operation of the divertor with no target would not be expected to lead to results much different from those obtained from operation without the divertor.

Experiments which emphasise the importance of the separatrix are summarised in Figure 6. The plasma column centre, R_p, is displaced by ΔR_p, so that the separatrix radius is varied, and the maximum current, I_p, attainable before instabilities appear, is recorded. These results were obtained with $B_\phi = 1.44T$. Assuming that the safety factor q at a radius a_q is restricting the current, a_q is given by

$$\left[\frac{1}{R} + \frac{1}{2I_p^o}\frac{\Delta I_p}{\Delta R}\right]^{-1}$$

where I_p^o is the maximum current with $\Delta R_p = 0$. A regression fit to the results demonstrates that $a_q = 0.21m$. Under these conditions $a_s = 0.175m$.

It appears that the safety factor at the separatrix restricts the plasma current, and $q_s \geq 2$ for stability. Without the divertor, $q_L \geq 2$ [24]: thus the separatrix is playing the role of a limiter in determining the current-carrying volume.

Throughout the experiments described here, it is the plasma electrical centre which is controlled by a vertical field feedback system. To maintain a constant separatrix radius, and scrape-off layer thickness, it is the geometric centre of the outer flux surfaces which should be controlled. For the measured plasma parameters, the difference between the two displacements is less than 5mm.

4 PARTICLE EXHAUST

Ionised particles in the scrape-off layer can flow into the divertor before reaching the limiters. These particles come from both the outward diffusion of the main plasma, and the ionisation of neutrals originating from external gas feed or desorption from the walls and limiters. As a consequence, for the same external gas feed rate, discharges with the divertor have lower density than those without the divertor. In order to maintain the same density in both cases, a feedback gas control system is used. Figure 7 shows the average density $\bar{n}_e$ with and without the control system in use. The change in the gas input rate between the two cases can, in principle, be used to determine the particle current to the divertor, but it requires the use of a recycling model (see Section 9), together with measurements of the confinement time. To overcome this difficulty, three techniques have been used to determine the particle current into the divertor. The first, ion saturation current measurements, provides a direct result. The second, density decay measurements, requires interpretation using

the continuity equation. The third, integration of density times velocity, requires a knowledge of the flow velocity. This latter technique is applied to the measured profiles both in front of the target and in the scrape-off layer, where a model for the divertor loss term is used.

The measured density profiles in the scrape-off layer are themselves determined by the divertor loss term, the ionisation source term, and the transport perpendicular to the magnetic field. Using a model for the divertor loss, which correctly predicts the diverted particle current, and a model for ionisation, a perpendicular diffusion coefficient is derived.

a) Ion saturation current

In this technique, the particle currents to the target and limiters are derived from the ion saturation currents. The current-voltage characteristic of the target plate, biased with respect to the vacuum vessel, is shown in Figure 8. Figure 9 shows the characteristics of a carbon limiter, again biased with respect to the vacuum vessel, for discharges with the divertor on and off. Plasma conditions were those described in detail in Section 8 and Table 4: I_p = 55kA, $\bar{n}_{eL}$ = 1.2 x 10^{19} m^{-3}, B_ϕ = 0.96T.

Saturation of the target plate characteristic was not obtained, so I^+_{SAT}(target) > 50A. Extrapolation suggests ~ 70A (4.4 x 10^{20} ions s^{-1}). Saturation of the limiter characteristic was obtained: I^+_{SAT}(limiter) = 17A with divertor and 24A without divertor. Assuming the ion flux in the torus is uniformly distributed over all limiters, I^+_{SAT}(limiters) = 150A (9.4 x 10^{20} ions s^{-1}) with divertor and 220A (1.3 x 10^{21} ions s^{-1}) without divertor. The total ion current is $\simeq$ 220A both with and without the divertor. Hence the particle confinement of the main plasma

is unaffected by the divertor but the divertor reduces the limiter current by 30%.

From the slope of the characteristic, the average temperature of the plasma impinging on the target is $T_e \simeq 40$eV. This value is consistent with the observation that saturation has not occurred with V = - 75V. The limiter characteristic can be used in a similar fashion giving a value of $\sim$ 14eV for the average electron temperature of plasma at the limiter. This is in reasonable agreement with probe measurements near the limiter for these discharges [16].

Caution must be exercised in relying solely on these results, because not all the consequences of biasing the target are understood. Biasing the target, but not the limiter, affects the density in the scrape-off layer: a positive voltage decreases the density measured with a Langmuir probe. Biasing the target can either increase or decrease the heat flux [25]. It is noted that the floating potential of both target and limiter is negative.

These experiments have been repeated at a lower density, $\bar{n}_{eL} = 7 \times 10^{18}$ m^{-3}, to give I^{+}_{SAT}(target) = 10A(6 x 10^{19} ions s^{-1}) and T_e (target) = 28eV [10]. These results are used for scaling of the particle current to the divertor with density, which is discussed later.

b) Density decay [13,18,19]

This method utilises the influence of the divertor on the ion flux to the limiters, and the fact that in a gettered torus with titanium limiters, particle induced desorption is much reduced. With no external gas feed the only particle flow into the plasma consists of neutrals with energies $\gtrsim$ 30eV. These originate from the neutralisation of ions, and their subsequent reflection as neutrals, at the limiter, and the reflection of fast neutrals at the walls. The mean free path for

ionisation of these neutrals is larger than the distance between the limiter and the separatrix, so there is negligible ionisation in the scrape-off layer.

A pre-determined external gas flow is used to obtain the required plasma density. The gas flow is stopped, and the resulting density decay observed. Without the divertor, the decay rate depends on the particle confinement time τ, and the reflection coefficient of the particles, β. With the divertor, the exhaust effect reduces the ion flux to the limiter, and consequently reduces the neutral flux back into the plasma. Thus the decay rate increases.

A simple model, including the neutralisation and reflection of ions, but neglecting the reflection of fast neutrals, is derived from the continuity equation. For $r = r_L = 0.26m$,

$$\frac{dN_L}{dt} = \frac{-N_L}{\tau_L} + S_L - I_D \qquad \ldots(1)$$

For $r = r_s = 0.175m$ (the separatrix position when the divertor is on),

$$\frac{dN_s}{dt} = \frac{-N_s}{\tau_s} + S_s \qquad \ldots(2)$$

Here the subscripts L, s, refer to the limiter and separatrix.

N_i is the total number of particles (ions) within a radius r_i

S_i is the ionisation source term within r_i ($S_L = S_s$)

I_D is the ion current to the divertor

$\frac{N_i}{\tau_i}$ is the outward ion current

$\bar{n}_{ei}$ is the average electron density within r_i

Defining the particle exhaust efficiency ξ_x as

$$\xi_x = \frac{I_D}{N_s/\tau_s} \qquad \ldots(3)$$

and assuming τ_s is unaffected by the divertor $(N_L - N_s)/N_L \ll 1$, and $\bar{n}_e \alpha N$, then

$$\frac{d\bar{n}_{eL}}{dt} = \frac{-\bar{n}_{eL}}{\tau_s}(1 - (1 - \xi_x)\beta) \qquad \ldots(4)$$

where β is the reflection coefficient for the ions.

A comparison of the decay rates with ($\xi_x > 0$) and without ($\xi_x = 0$) the divertor then gives ξ_x and τ_s. A value $\beta = 0.5$ is used, which has previously been shown to correctly predict the density behaviour in DITE [11]. Corrections are made for the reflection of neutrals and incomplete gettering ($\sim$ 80% wall coverage).

Figure 10 shows results obtained, in deuterium, with $\bar{n}_{eL} = 1.2 \times 10^{19}$ m^{-3} (other conditions are as described in Table 4). The value of $\ell n(\bar{n}_{eL})$, as a function of time after the external gas flow is stopped, shows that the divertor increases the decay rate by 30%: τ_s = 14ms and $\xi_x = 0.3$, so that I_D = 48A (3×10^{20} ions s^{-1}). Repeating the experiment with $\bar{n}_{eL} = 8 \times 10^{18}$ m^{-3} gives τ_s = 14ms and $\xi_x = 0.15$: I_D = 16A (1×10^{20} ions s^{-1}).

c) Integration of density timesvelocity [10]

The total particle current to the target is evaluated from $\int n_e v_{||}$ over the target plate, where $v_{||}$ is the flow velocity along the field lines. With $\bar{n}_{eL} = 6 \times 10^{18}$ m^{-3} in hydrogen, densities $\sim 5 \times 10^{17}$m^{-3} have been measured in front of the target both with a Langmuir probe and an 8mm microwave system. Figure 11 shows the variation of n_e across the target plate, on the line Z = 0, 2cm in front of the plate. The e-folding distance is $\sim$ 5cm, compared with $\sim$ 3cm in the scrape-off layer. This difference is explained by the changing magnetic field configuration as the field lines are followed into the divertor and onto the plate.

Electron temperatures $\sim$ 28eV are deduced from the current-voltage characteristic of the target plate biased to the vacuum vessel. Assuming $T_i = T_e$ and $v_{||} = 0.4\ (T_i/m_i)^{\frac{1}{2}}$, [26], a value consistent with other experiments [27,28 and Section 6], the ion current to the target is 10A (6×10^{19} ions s^{-1}).

The particle current to the divertor can also be calculated from the measured density and temperature profiles in the scrape-off layer, if a model for the flow into the divertor is used. Figure 12 shows the electron density profile, divertor on and off, obtained from the microwave system, the Thomson scattering system, and a Langmuir probe. Figure 13 shows the electron temperature profile, divertor on and off, obtained from the Thomson scattering system and the Langmuir probe. Both profiles were obtained with plasma conditions as listed in Table 4: $\bar{n}_{eL} = 1.2 \times 10^{19}$ m^{-3}. With the divertor on the density e-folding distance in the scrape-off layer is 50mm. This is reduced as $\bar{n}_{eL}$ is reduced. The temperature e-folding distance is 40mm and independent of density.

A model for the particle flux into the divertor has been developed

[29,30] in which it is assumed the ions are collisionless over the scale length of the divertor chamber, but collisional over the total field line length in the scrape-off layer. This is consistent with the experimentally measured parameters. The model includes the magnetic mirror at the divertor throat, which reflects ions outside the 'loss cone' back into the main chamber, and decreases the electrostatic potential between the throat and the plate. The effects of neutral gas in the chamber on the electrostatic potential are ignored. The particle current to the divertor, I_D, is then given by

$$I_D = 4\pi \int_{a_L}^{a_s} \frac{1.6\ n_e}{M\ q_D} \left(\frac{kT_i}{2\pi m_i}\right)^{\frac{1}{2}} rdr \qquad \ldots(5)$$

Assuming $T_i(r) = T_e(r)$, $n_i(r) = n_e(r)$, and including the computed dependence $q_D(r)$, the expression is evaluated to give $I_D = 96A(6 \times 10^{20}$ ions $s^{-1})$ with $\bar{n}_{eL} = 1.2 \times 10^{19}\ m^{-3}$, and $I_D = 24A(1.5 \times 10^{20}$ ions $s^{-1})$ with $\bar{n}_{eL} = 7 \times 10^{18}\ m^{-3}$.

Figure 14 shows the combined results of the above experiments, presented as the particle current to the divertor as a function of the average density. The values deduced from the density decay experiments represent only the flux from outward diffusion of the main plasma, and are expected to be smaller than the values derived from the other techniques. The values obtained from the measured profiles in the scrape-off layer are approximately 40% greater than those derived from the ion saturation current technique.

Measurements of the flux of deuterium ions and atoms from the plasma have been made using a thermal desorption probe[31]. These give a value of 2×10^{20}

particles s^{-1} (32A), assuming that the flux is uniform around the torus. This is only about 15% of that deduced from the ion saturation current and density decay experiments. The discrepancy is not understood.

d) The electron density profile

The form of the electron density profile in the scrape-off layer, used to deduce the parallel ion flux leaving the main torus, is determined by the parallel loss, a radial particle velocity (or equivalent diffusion coefficient $D_\perp$), and the ionisation of neutrals.

The continuity equation for a constant electron density can be written in cylindrical geometry as

$$\frac{1}{r}\frac{\partial}{\partial r}\left(r\, D_\perp \frac{\partial n_e}{\partial r}\right) = \frac{n_e}{\tau_\parallel} - n_e\, n_n\, \langle\sigma v\rangle \qquad \ldots(6)$$

where $\tau_\parallel$ is the characteristic time for ions to reach the divertor, n_n is the neutral particle density and $\langle\sigma v\rangle$ the ionisation rate coefficient. To interpret the profiles in Figure 12, a form for $D_\perp$ must be assumed. We take $D_\perp = k/n_e$ as has been suggested elsewhere [33]. With the divertor off, the radial dependence of the source term $n_e\, n_n\, \langle\sigma v\rangle/k$ can then be derived, and is shown in Figure 15a. Most of the ionisation is outside a radius of 0.2m, consistent with the majority source being from gas feed and desorbed hydrogen. Also shown in the figure is the computed source term resulting from the input of molecular deuterium neglecting recycling from the limiters. The three competing processes of molecular dissociation followed by atomic ionisation, are considered using the measured external gas flow rate of 7×10^{20} molecules s^{-1} and the measured density profile. The source term calculated from the two methods agree well if $k = 2.6 \times 10^{18}$ $m^{-1}\, s^{-1}$ is assumed, as shown in Figure 15a.

With the divertor on, the term $(n_e\, n_n\, \langle\sigma v\rangle - n_e/\tau_{||})/k$ can be derived, and is shown in Figure 15b. The source term in the scrape-off layer is now balanced by flow into the divertor. There is a small source inside the separatrix which may result from recycling of the working gas near the stagnation point or, more likely, reflect the large errors involved in the double differentiation of a density profile obtained from line of sight measurements.

If we assume the source term $n_n\, n_e\, \langle\sigma v\rangle$ and the diffusion constant k are unaffected by the divertor then the term $n_e/(k\tau_{||})$ can be obtained, and this is shown in Figure 15c. Integrating this gives a value for I_D/k. Using the value of I_D from Figure 14, a value for k of 2.3×10^{18} $m^{-1}\, s^{-1}$ can be derived. That is, this value of k closely predicts the measured total particle current to the divertor.

The broken line in Figure 15c represents the spatial dependence of the term $n_e/(k\tau_{||})$ derived from a model for the parallel loss from the main torus [29,30] and $k = 2.3 \times 10^{18}$ $m^{-1}\, s^{-1}$.

The above analysis demonstrates that the measured density profiles and parallel ion loss are consistent with a diffusion coefficient $D_\perp = k/n_e$, ($k \sim 2.5 \times 10^{18}$ $m^{-1}\, s^{-1}$), the measured external gas input, the ionisation model and the model for the particle flux to the divertor. The value of k is approximately 1/6 of that used for INTOR modelling [32]. At the separatrix $D_\perp \sim 0.1\, D_{Bohm}$, at the limiter $D_\perp \sim D_{Bohm}$ and behind the limiter, the density profiles can be predicted using $D_\perp \sim D_{Bohm}$. In Figure 12, the solid lines represent the predicted density profiles obtained from the above assumptions, normalised at r = 0.175m. The agreement with experiment implies that more comprehensive one-dimensional computer calculations of the scrape-off layer will be useful.

To conclude this section on particle exhaust, Table 2 summarises the particle currents to the limiters and divertor, together with the coefficients which correctly predict the density.

5 ENERGY EXHAUST

One of the properties of a divertor is the removal of energy from the scrape-off layer, with a consequent cooling of the plasma edge. This will reduce the sputtering of impurities from the limiters.

The energy (and power) to the divertor has been measured using an infra-red camera [17], and an array of thermocouples mounted on each of the target plates. Figure 16 shows examples of the contours of power on the electron drift side, with $\bar{n}_{eL} = 6 \times 10^{18}$ m^{-3}. The crescent shaped contours correspond to the diverted field line structure, the density contours, and the damage on the target (Figure 4). Power densities up to 20MW m^{-2} have been recorded on the electron drift side with low plasma electron densities ($\sim 2 \times 10^{18}$ m^{-3}). Cine photography under these conditions shows that material is removed from the target; the target shown in Figure 4 is perforated at the position where the separatrix intersects the plate.

Figure 17 shows the maximum temperature rise recorded by the thermocouple array, for each of the target plates (designated electron and ion drift sides). For densities $\bar{n}_{eL} \lesssim 6 \times 10^{18}$ m^{-3}, the electron drift side reaches a higher temperature, suggesting the presence of supra-thermal electrons. Figure 18 shows the fraction of ohmic power,

P_Ω, reaching the plates. For these discharges P_Ω was between 80 and 100kW. For $\bar{n}_{eL} \gtrsim 8 \times 10^{18}$ m^{-3} the deposition profile broadens. Typically, 10% of the ohmic power reaches the divertor target.

The average energy of the particles impinging on the plate can be deduced from the power and particle fluxes. This is shown in Table 3, and varies from $\gtrsim$ 4keV at the lowest densities, to 150eV for $\bar{n}_{eL} = 1.2 \times 10^{18}$ m^{-3}.

Assuming an average temperature in the scrape-off layer of 25eV over this density range, the parameter

$$\gamma = \frac{\text{Power to target}}{\text{Particle current to target x temperature in scrape-off layer}} \quad (7)$$

can be evaluated: results are shown in Table 3. γ varies from $\sim$ 150 at the lowest densities, to $\sim$ 6 for $\bar{n}_{eL} = 1.2 \times 10^{19}$ m^{-3}. Results obtained with the MkIA [10] gave $\gamma \sim 200$, about 10 times larger that that obtained with the MkIB at the same density (see Section 12).

Models for the heat flux to a target have been developed [29,30, 33 and references therein]. The most applicable [29,30] include the effect of the sheath potential; the bundle divertor magnetic mirror and subsequent magnetic well also increase the potential in the scrape off layer relative to the target. For the DITE parameters this gives γ = 8.6 in a deuterium plasma, neglecting the effect of secondary electron emission. Secondary electrons will decrease the sheath potential, and increase γ to $\sim$ 10 [25].

For the higher density discharges ($\bar{n}_{eL} \sim 1.2 \times 10^{19}$ m^{-3}) there is agreement to within 50% between the measured and predicted values of γ.

That is, the measured power is consistent with the measured (and predicted) particle flux, the measured temperature, a thermal velocity distribution and an electrostatic sheath.

At the lowest densities the measured value of γ is about 15 times that expected. Taking the theoretical distribution of the particle flux, together with the measured distribution of temperature in the scrape-off layer, it can be shown that the largest discrepancy between the predicted and measured power distribution at the target occurs near the separatrix. One explanation for this discrepancy is the presence of suprathermal electrons. These carry more energy to the plate. Also a higher secondary electron coefficient, from the higher energy electrons, will increase the expected value of γ. The presence of suprathermal electrons and their ability to transport large energies has been shown to correctly predict results on the DIVA tokamak at low electron densities [23]. On DITE, the observation that the majority of the power is deposited on the electron drift side at low densities supports this explanation.

For intermediate densities, the measured value of γ is about twice that predicted. The experiments indicate an equal energy distribution on the ion and electron drift sides, suggesting no suprathermal electrons. However, the experimental values of γ quoted are obtained from total values of particle currents and powers, and an average temperature. Spatial dependences must be used if more accurate results are required.

The results from the MkIA divertor, in which a value of $\gamma \sim 200$ was deduced, suggest that a high proportion of suprathermal electrons were present under the conditions then prevailing.

It is noted that the application of the divertor fields, even at a level such that the separatrix is only 10mm inside the limiters ($a_s = 0.25$m), reduces the hard X-ray flux (energies $\gtrsim$ 50keV). This is recorded with a SiLi diode detector, and implies a reduction in the population of high energy electrons by the perturbing fields.

One of the consequences of the energy flow to the divertor is a cooling of the plasma edge. Experimentally, the electron temperature at the limiter radius is reduced from ~ 15eV to ~ 10eV, when $\bar{n}_{eL} = 1.2 \times 10^{19}$ m^{-3}, when the divertor is used. In principle, the temperature profiles with and without the divertor should allow a calculation of the perpendicular electron thermal conduction coefficient, as was performed for the particle diffusion coefficient in Section 4e. However, the large uncertainties in the sources and losses in the scrape-off layer prohibit this.

Power balances have been obtained from detailed profile measurements and the results are summarised in Figure 19 for a gettered torus, titanium limiters, and $\bar{n}_{eL} = 1.2 \times 10^{19}$ m^{-3}. The conducted and convected power is deduced from the difference between the measured ohmic power and radiated power (plus charge exchange losses). Of the power conducted and convected across the separatrix, 15% (8kW) reaches the target plate. With the MkIA at low densities, $\bar{n}_{eL} = 6 \times 10^{18}$ m^{-3}, this value was $\gtrsim$ 80% [see Section 12].

The power conducted and convected to the limiters is 43kW (see Figure 19). The average energy of the incident ions can be evaluated from the measured particle fluxes to the limiters. This is 200eV without the divertor, and 300eV with the divertor. An approximate value of γ can then be derived from the plasma temperature at the limiters: $\gamma = 30$ with the divertor and 13 without the divertor. The expected value is $\simeq 10$. In the case of a non-gettered torus, the measured energy and particle fluxes, and the measured temperature and density profiles behind the limiter are consistent with a value of $\gamma = 10$ [16]. The large value derived for the case with a gettered torus and the divertor on is not understood, but may reflect errors in the conducted and convected power. Another possibility is that the ion temperature is significantly higher than the electron temperature in the scrape-off layer. Experimental evidence for this has been obtained

from carbon collector probes at typically 0.24m radius in the torus. Values of $T_i \sim 50eV$ have been measured.

The measurements of the power to the target take no account of any energy lost to the target chamber walls, and this measurement therefore gives a lower limit to the power flow to the divertor. An alternate method is to deduce the conducted and convected power from the limiter temperature rise. This gives $\simeq$ 30kW. The power to the divertor must then be the difference between the ohmic input power and the sum of the conducted, convected and radiated powers. The power to the divertor is then $\sim$ 20kW, suggesting that $\sim$ 12kW are deposited on the chamber walls. However, there are very large errors involved in the measurement of the limiter temperature rise and its interpretation as an incident power. Bolometric measurements within the target chamber are required to understand any role played by radiation and charge exchange phenomena.

6 IMPURITY SCREENING

Impurities originating from the vacuum vessel walls and limiters may become ionised in the scrape-off layer, and swept into the divertor before penetrating the main discharge. We define a screening, or shielding, coefficient ξ_s:

$$\xi_s = \frac{\text{impurity particle current to divertor}}{\text{impurity particle current into the scrape-off layer from the plasma edge}} \quad \ldots(8)$$

Direct observations of impurity currents into the divertor have not been made. Instead, the shielding coefficient is deduced by comparing discharges with and without the divertor. Assuming that the

inward transport is not affected by operating the divertor, then

$$\xi_s = 1 - \frac{\text{impurity particle current into main plasma, divertor on}}{\text{impurity particle current into main plasma, divertor off}} \quad ..(9)$$

It is this definition which is also used in Section 8 and 9.

Measurements have been made of the effect of the divertor on impurities intrinsic to the tokamak. These are low Z-carbon and oxygen existing as impurities in the walls and limiters, and high-Z titanium and iron, from the limiter and wall material itself. Several other effects besides screening of impurities, combine to reduce the impurity content. The plasma periphery is affected, for example, by the additional external gas feed required to maintain the density when the divertor is operated. This will affect the plasma wall and plasma-limiter interaction. Early data on intrinsic impurity screening [8] were corrected for the change in source function by measuring the change in impurity flux at the wall. However, recent data show gross poloidal and toroidal asymmetries in impurity radiation, implying local impurity sources, complicating the analysis. The metal impurity concentration in the boundary layer has been measured using rotating collectors which are subsequently analysed by Rutherford Backscattering. The largest fluxes are of titanium and iron. The radial distribution of titanium decreases from typically 5×10^{18} ions m^{-2} s^{-1} at 0.23m to 2×10^{18} ions m^{-2} s^{-1} at 0.26m. The values of the iron flux are typically a factor of 2 to 3 lower. Assuming that the impurities are in equilibrium with the plasma ions a flux of 5×10^{18} m^{-2} s^{-1} to a collector is equivalent to a density of 2×10^{14} m^{-3}. The time behaviour of these fluxes shows

a slow decay from a maximum during the rising current phase (Figure 20). This maximum is correlated with a high plasma flux to the limiter. Without the divertor, measurements have been made from 0.26-0.27m radius. The titanium flux at 0.26m is $\sim 5 \times 10^{18}$ m^{-2} s^{-1} ie, comparable with that at 0.23m with the divertor on. This is consistent with the higher plasma density and temperature at the limiter with the divertor off. No major differences in the impurity concentrations are observed between divertor on and divertor off within the accuracy of the measurements.

Recent impurity screening measurements [15,18] have involved injecting identical small amounts of extrinsic impurities into plasmas produced both with and without the divertor. No investigation of any variation with injection position has been made. Two methods have been used: laser ablation [35] and gas puffing. Using a 2J Q-switched ruby laser, up to 3×10^{17} atoms of aluminium, with energy $\sim$ 3eV, have been injected. No spectroscopic flux measurements have been made, but X-ray measurements of the He-like Al XIV line (1.6keV) show little difference between the Al 13+ concentrations at the plasma centre whether the divertor is on or off. However, the sensitivity of the emission to variations in electron temperature implies an error $\sim$ 50% in the derived concentrations. Measurements of the injected aluminium on the surface probe gave fluxes $\sim 2 \times 10^{20}$ m^{-2} s^{-1} at radii of 0.22m 0.24m. The flux decayed typically over a time of 50ms. A less direct approach uses the measured increase in electron density associated with the ionisation of the injected atoms; from charge neutrality the concentration of aluminium can be estimated. This technique implies that the divertor reduces the concentration of aluminium by 30%. A similar value is derived from the increase in plasma resistivity, produced by ionisation, cooling and impurity content

increase. With $\bar{n}_{eL} = 1.2 \times 10^{19}\ m^{-3}$, and the divertor off, only 10% of the injected material reaches the hot plasma. This is reduced to 7% with the divertor on.

By observing the time history of an Al III line (360.1nm), at points close to, and 180° in major azimuthal angle from, the point of injection, a flow velocity of $1.25 \times 10^{4}\ ms^{-1}$ along the field lines has been measured. This is approximately equal to the value $0.4 \left(\frac{T_e}{m_D}\right)^{\frac{1}{2}}$, where m_D is the deuterium ion mass and suggests that both the working gas and impurity ions have the same flow velocity along the field lines.

Gas puffing through a piezoelectric valve has been used to inject neon and argon for times between 20 and 50ms. The quantities correspond to ~ 1% of the total electron concentration. Observations of the Ne VIII (77.0nm) and A VIII (70.0nm) lines have been made. Calculations of ionisation rates show that these ion states occur in the region where T_e > 100eV: ie, in the main plasma. The line intensities are interpreted as fluxes, because the particular states observed should be completely ionised to the next state along the line of sight of the spectrometer, and the temperature and density profiles (Figures 12 and 13) are almost unchanged by the divertor. Such an interpretation has been shown to be correct in certain cases [36].

Figure 21 shows the variation of the Ne VIII line intensity with average density, $\bar{n}_{eL}$, divertor on and off. The line intensity increases with increasing density both with divertor on and off. If the interpretation of this intensity as a flux is correct, this observation suggests that the impurity diffusion in the outer regions of the plasma decreases with increasing electron density [37].

Using the definition of the screening coefficient, equation 9, we can write

$$\xi_s^{Ne} = 1 - \frac{\text{Ne VIII line intensity, divertor on}}{\text{Ne VIII line intensity, divertor off}} \qquad \ldots(10)$$

Figure 22. shows ξ_s^{IMP} as a function of $\bar{n}_{eL}$ from the neon and argon puffing experiments. The results show ξ_s^{IMP} increases with increasing average density, and thus with increasing density in the scrape-off layer. The maximum value measured is $\xi_s = 0.38$ with $\bar{n}_{eL} = 1.3 \times 10^{19}$ m^{-3}.

The simplest model which may be used to estimate the screening assumes that all impurities ionised in the scrape-off layer are swept into the divertor [3]. With the measured density and temperature profiles this would imply $\xi_s^{IMP} \geq 0.9$ for all the experimental conditions. The experimental values are at least a factor 3 smaller than this, which can be explained if an inward transport mechanism exists, allowing ions to cross the scrape-off layer before reaching the divertor.

Estimates for the screening efficiency expected from neoclassical theory have been made. The ions are assumed to experience sufficient collisions for the influence of the bundle divertor magnetic mirrors to be neglected [3]. The continuity equation (including the parallel ion loss to the divertor [29,30]) is solved [38] and predicts $\xi_s^{IMP} \sim 1$.

Estimates can be made for the diffusion coefficient required to explain the experimental observations. Assuming a spatially independent anomalous impurity diffusion coefficient, $D_\perp^{IMP}$ and a spatially independent divertor loss time $\tau_{||}^{IMP}$, the continuity equation is solved to give

$$\xi_s = 1 - \exp - \left(\frac{a_L - a_s}{(D_\perp^{IMP} \tau_{||}^{IMP})^{\frac{1}{2}}} \right) \qquad \ldots(11)$$

Using the following expression for $\tau_{||}$ (assumed the same for impurities as working gas ions):

$$\tau_{||} = \frac{\pi R M q_D}{1.6 (kT_e)^{\frac{1}{2}} / (2\pi m_i)^{\frac{1}{2}}} \qquad \ldots(12)$$

where m_i is the deuterium mass, we obtain, for typical values (see Table 1), $\tau_{||} \sim 5$ms. With $\xi_s = 0.3$, equation (11) gives $D_\perp^{IMP} \simeq 10\ m^2\ s^{-1}$, or an inward velocity $\simeq 50 m\ s^{-1}$. The fact that ξ_s^{IMP} increases with density suggests either that $D_\perp^{IMP} \propto 1/n_e$, or that the radius at which ionisation occurs increases as the electron density is increased.

Results obtained with the MkIA divertor were deduced from the intrinsic impurity behaviour. The screening efficiency was deduced from the equation

$$\xi_s^{IMP} = \frac{\text{Impurity line intensity, } r < a_s, \text{ BD on}}{\text{Impurity line intensity, } r < a_s, \text{ BD off}} \times \frac{\text{Impurity line intensity, } r \sim a_L, \text{ BD off}}{\text{Impurity line intensity, } r \sim a_L, \text{ BD on}} \qquad \ldots(13)$$

Results from oxygen (OVII and OII) gave $\xi_s \sim 0.5$ with $\bar{n}_{eL} \sim 8 \times 10^{18}\ m^{-3}$, about twice the value deduced for neon from the gas puffing at a similar density. Results for metals were obtained from a combination of XUV spectra and carbon probe data. Figure 23 shows XUV spectra

obtained, with $\bar{n}_{eL} \sim 7 \times 10^{18}$ m^{-3} [6]. A dramatic reduction in line radiation from high Z impurities is seen when the divertor is operated, implying a large reduction in metal fluxes into the plasma core. The corrections for changes in source function at the walls and limiters were made by observing the change in metal impurities collected on a carbon probe, inserted at the plasma periphery, as shown in Figure 24. Values for the screening of the metals, $\xi_s^{Mo,Fe} \sim 0.8$, are deduced, much larger than obtained with MkIB during aluminium and argon injection experiments. Even if the known asymmetries in line radiation emanating from the plasma periphery bring into question the validity of this result, the fact remains that a much larger reduction in metal line radiation was observed in the MkIA than the MkIB (see Section 8). Some discussion of possible reasons for this is presented in Section 12.

7 PARTICLE RETENTION

In the previous section it was tacitly assumed that no particles entering the divertor returned to the main torus. Experiments have been performed in which neon and deuterium were puffed into the divertor chamber during discharges both with and without the divertor. The resulting density increases in the main plasma were measured. With no pumping in the target chamber (ie, no gettering of the walls) operating the divertor reduced the density increase to 30% of that obtained without the divertor. The addition of neutral gas into the chamber may have adversely affected the divertor operation, by reducing the potential drop between the main chamber and the divertor chamber [29].

A topic related to particle retention is erosion of the target plate. Arc tracks have been observed on both the electron and ion drift sides of the target, in addition to localised melting (Figure 4) on the

electron drift side when operation with low plasma densities was undertaken. However, measurements of the plate thickness after 283 discharges showed no erosion on the ion drift side; the errors place an upper limit of 20nm per discharge.

A more sensitive technique used was to activate a small piece of titanium by bombardment with 7Mev protons [39]. The resulting ^{48}V decays by positron emission, producing X-rays, with a half life of 16.2 days. This material was attached to the target, and the decay in activity recorded over a number of discharges. The results indicated an erosion rate of 3.5 ± 0.7nm per discharge, about 100 times that expected from sputtering. Arcing is the most probable source of erosion. However arcing does not always take place and the conditions under which it does and does not occur are not yet understood.

8 A COMPARISON OF PLASMAS PRODUCED WITH AND WITHOUT THE DIVERTOR

The previous sections have described in detail measurements of the different divertor functions. This section describes their combined effect on the overall plasma behaviour with and without the divertor. In comparing discharges with and without divertor, the limiters are kept at $a_L = 0.26m$, and the average density $\bar{n}_{eL}$ is kept constant.

Detailed comparisons have been made, using the MkIB divertor, with $\bar{n}_{eL} = 1.2 \times 10^{19}\ m^{-3}$, and Table 4 lists measured and derived plasma parameters. These discharges have been referred to throughout the text: Figure 12 shows the electron density profile, Figure 13 the electron temperature profile, and Figure 19 the energy balance. Results have been compared both with and without titanium gettering of the vacuum vessel walls. Gettering reduces the oxygen impurity line intensities [22], the X-ray (A_x) and resistance anomaly factors, and radiated

power, P_{RAD}.

To keep the density constant, additional gas is required when the divertor is on. A greater increase is required for a non-gettered torus than when gettering is used. Without gettering, refuelling is dominated by recycling from the walls and limiters. With gettered walls, the recycling from the walls is reduced, and the external gas input dominates. Because the divertor does not greatly affect the ionisation source term (see Section 4d), only a small increase in the external flow rate is required (~ 30-50%).

We consider first the discharges without titanium gettering. The divertor does not affect the radiated power, which is ~ 90% of the ohmic input power. The X-ray anomaly factor on axis is reduced by a factor ~ 4, and there is a 20% reduction in $(Z_{eff}-1)$. Impurity line radiation intensities have been monitored: these show no change in the OVII line (162.4mn), and a 30% reduction in Ti XIV (211.8mn). This constancy of the oxygen line intensities was also observed with the MkIA [8]. Measurements of carbon impurities show a reduction in line intensity (CV, 227.2nm) but these results are deduced from 2 discharges only.

In discharges with titanium gettering, the radiated power is reduced by 35% by gettering, and a further 35% by the divertor. The resistance and X-ray anomaly factors are both reduced by the gettering and further reduced by the divertor. Gettering reduced the OVII line intensity by a factor ~ 4, and the TiXIV line intensity by factor ~ 2: no information on the effect of the divertor on these lines is available.

Comparisons of discharges with and without the MkIA divertor (with densities $\bar{n}_{eL} \sim 7 \times 10^{18}$ m^{-3}, not gettered) were obtained, with the moveable limiters at 0.27 and 0.19m when the divertor was off [7]. Large reductions in line intensities were observed (Figure 23), by a factor of 3 to 10 for iron, 20 to 50 for molybdenum, and 30% to 50% for carbon and oxygen [12]. The largest reductions were observed for lines originating just inside the separatrix. Figure 25 shows the profiles of radiated power obtained [8]; the total power was reduced by a factor ~ 5. At the same time, the X-ray anomaly factor was reduced from ~ 700 to ~ 70 [40], the central peak in the radiation profile and the large value of X-ray anomaly factor are correlated to the molybdenum impurity from the limiters. Obviously, the conditions then prevailing produced more dramatic results than obtained with the MkIB device. Possible explanations, concerned with density variations, instabilities and suprathermal electrons, are discussed in Section 12.

9 A GLOBAL MODEL FOR IMPURITY PRODUCTION

The experimental results described in Section 6 show that both high and low Z extrinsic impurities are screened by the divertor. The comparisons presented in Section 8 show that intrinsic impurities are reduced. To understand these comparisons, a global model of impurity production has been developed [15], based on the model previously used to estimate recycling of the working gas [11].

In the model, the plasma is divided into 2 regions, an inner core with $r < a_s$ and a scrape-off layer $a_s < r < a_L$. Particles enter the plasma, penetrate the hot core, and return to the edge with a confinement time $\tau_s = N_s/I_s$ evaluated at a_s. Here I_s is the particle current across the separatrix. When the divertor is operated, fluxes into the

scrape-off layer are depleted by parallel flow to the target plates. Screening and exhaust efficiencies are defined by equations 9 and 3 respectively. For the working gas, the screening efficiency is that fraction of the incoming gas which is ionised in the scrape-off layer; once ionised it is lost to the divertor with the exhaust efficiency. Although this model is too simple, and one dimensional transport calculations should be performed, some insight into the divertor operation is gained, and areas of ignorance highlighted.

The mechanisms for impurity production considered here are illustrated in Figure 26, and the relevant coefficients listed in Table 5. Low Z impurities, present as a surface contamination on the walls, are desorbed by the fast neutrals. Gettering is assumed to reduce the surface concentration. Ions impinging on the metal (heavy, or high Z) limiters will deplete the light impurity concentration in times much less than the discharge time. The returning low Z impurity ions are assumed to be trapped in titanium limiters, but recycled at molybdenum limiters. Thus for titanium the effective desorption yield is zero.

Metallic impurities are assumed to be produced by four sputtering sources. These are (a) the flux of working gas ions to the limiters, with an energy of the sheath potential, (b) the charge exchange neutral flux to the walls, with an energy equivalent to the ion temperature at a distance of one mean free path for charge exchange from the walls, (c) the low Z ion flux to the limiters, with an energy of the charge state times the sheath potential, and (d) the high Z ion flux to the limiters, with an energy of the charge state times the sheath potential. The charge state is not known; values of 1 and 4 are assumed. The value 4 is consistent with an analysis of the titanium deposition profile on a disc behind a small aperture, inserted into the plasma periphery

[43,44]. The effective ion energy is derived from the analysis of trapped deuterium on a carbon probe [14], and is ~ 50eV in non-diverted discharges. Arcing has been neglected, because experiments show it to be important only during the plasma formation [45].

For equilibrium at a constant density, the equations determining the recycling of the working gas can be solved analytically to give the fast neutral flux Γ_o in terms of the ion flux, Γ_i across the separatrix. Writing $\Gamma_o = \alpha\ \Gamma_i$, the light and heavy impurity fluxes are then given by:

$$\frac{\Gamma_L}{\Gamma_i} = F[1 - \xi_s^L][\alpha y^o + (1 - \xi_x^i) y^i] \qquad \ldots(14)$$

$$\frac{\Gamma_H}{\Gamma_i} = \frac{1 - \xi_s^H}{1 - (1 - \xi_s^H)(1 - \xi_x^H)\ S^H} \Big[\alpha S^o + (1 - \xi_s^L)(1 - \xi_x^L)\ S^L F(\alpha y^o +$$

$$(1 - \xi_x^i)\ y^i) + (1 - \xi_x^i)\ S^i\Big] \qquad \ldots(15)$$

Here the subscript or superscript j = o,i,L,H, refers to neutrals, hydrogen ions or light and heavy impurities. y^o, y^i are the desorption yields of light impurities by neutrals and ions, S^j the sputtering yields of heavy impurities by species j, and F the fraction of the wall area not covered by active titanium. Values used are quoted in Table 5.

The parameter $\alpha = \Gamma_o/\Gamma_i$, the number of charge exchange neutrals leaving the plasma per hydrogen ion, is shown in Figure 27 as a function of the shielding efficiency ξ_s^i for two extremes of exhaust, ξ_x^i = 0 and 1.

The figure shows that the fast neutral flux to the walls is increased by less than 5% (at constant plasma density) when the divertor is operated, ($\xi_s^i \sim 0.8$). For titanium limiters, equation 14 then shows that the reduction in light impurities should be $\sim \xi_s^L$, or 30%. This is at variance with the observation of constant oxygen line intensity, but in agreement with the restricted carbon data (see Section 8). The model predicts no change in the fast neutral flux ($\alpha \sim$ constant), thus no change in the oxygen source. This is in agreement with the observed constancy of the OII line intensity: however known asymmetries make this observation of doubtful value.

An explanation for the anomalous behaviour of oxygen may involve an oxygen source near the stagnation axis; the oxygen could penetrate the main plasma without passing through the separatrix. (Carbon data may be different because of the presence of the moveable carbon limiters, but the effect has not been evaluated.) Direct observations near the stagnation axis are required. A consequence would be the reduction of line intensities from intermediate charge states of oxygen, OIII to OVI; such results have been obtained, and are shown in Figure 28. However, the gettering of the torus walls in the area around the stagnation axis makes a large oxygen source unlikely.

Equation 15 predicts the fluxes of high Z impurities into the plasma core. The first term results from neutral sputtering, the second, from light impurity sputtering, and the third, from hydrogen ion sputtering. The denominator results from the enhancement produced by self-sputtering of the heavy impurities. Using the coefficients in Table 5, for a device with titanium limiters and walls (MkIB), the sputtering from neutrals is dominant, and the divertor should reduce the flux by $\sim \xi_s^H$, or 30%, as is observed [see Section 8].

For a device with limiters and walls of different materials (MkIA) the reduction in heavy impurities from the walls would again be $\sim \xi_s^H$, or 30%. However, for the heavy impurities from the limiters, the dominant term is either from hydrogen ion sputtering or light-heavy sputtering, depending on the impurity charge state. The reduction would then be between 50% and 70%. The results from the MkIA showed much larger reductions typically by a factor 10, in both iron (from the walls) and molybdenum (from the limiters). Results also show the iron concentration to be larger than the molybdenum concentration [6], in agreement with the prediction of the model that the neutral flux to the walls is larger than the ion flux to the limiters. However such conclusions are tentative as it has been shown that significant amounts of iron ($\sim 10^{17}$ atoms cm^{-2}) become uniformly deposited on the limiters after a short period of operation.

Table 6 summarises the impurity data, both experimental and predicted. Predictions for the MkIA are based on coefficients applicable to the MkIB at a higher density, which will over-estimate the flux reduction. The disagreements reflect the uncertainties in the model: in particular the energy of the impurities reaching the plasma edge, and any change in this when the divertor is operated. Further progress awaits experiments to determine which, if any, of the proposed impurity production mechanisms are dominant.

10 NEUTRAL INJECTION

One of the objectives of DITE is to study the effects of neutral hydrogen beam heating. An advantage of operating with a divertor is that the particle flux to the limiters is reduced, resulting in density control without the use of titanium gettering, as well as

impurity reduction. One problem which may arise is the loss of high energy ions because of the magnetic field perturbation introduced by the divertor.

Initial beam heating experiments with the MkIA divertor [12] used 0.2MW of injection power, with trapping efficiencies of up to 50%. There was a large increase in impurity line radiation, which the divertor did not affect. The clearest results have been obtained with the MkIB device, where higher densities and currents mean that the neutral beam is more effectively trapped. Impurity data has been obtained with $B_\phi \simeq 1T$, while energy exhaust measurements have been obtained with $B_\phi = 1.44T$.

With 400kW of hydrogen (energy ~ 20keV) injected into a deuterium plasma (in the same direction as the plasma current) the temperature changes shown in Table 7a were obtained. Plasma conditions were similar to those listed in Table 4. The ion temperatures, obtained from the analysis of the radial charge exchange neutrals, show no significant change in the heating with and without the divertor. Large increases in line radiation (by factors ~ 3 for oxygen) have been observed, which have been shown to be due to charge exchange recombination processes [46]. The results are consistent with the increased line radiation originating from impurities already present in the plasma, rather than from an increased influx from the walls and limiters. Any reduction in radiated power during injection brought about by operating the divertor is less than 25%.

The temperature increases shown in Table 7b were obtained when operating the MkIB at higher toroidal fields (see Table 1). Again there is no significant difference in the heating whether the divertor is on or off. Under these conditions the temperature rise of the target

plates has been measured using thermocouples. Without injection, the temperature rise corresponds to an incident energy of 2kJ, for an ohmic power P_Ω = 160kW and radiated power P_R = 100kW. For the measured divertor current pulse length of ~ 200ms, approximately 17% of the conducted and convected power reaches the target plates, similar to that previously observed [15%; see Section 5]. With 400kW of neutral injection for 100ms the energy incident on the target is 4kJ. The ohmic power drops from 160kW to 100kW and the radiated power increases from 100 to 200kW during injection. A total of 36kJ is lost by conduction and convection, of which 11% appears at the target.

We now discuss three possible loss mechanisms resulting from the operation of a bundle divertor on a tokamak. Associated with the bundle divertor is a magnetic field perturbation, localised in toroidal angle. This perturbation is 100% at the stagnation axis, and about 3.5% at the vacuum vessel centre with both the MkIA and MkIB divertors. The effect of this ripple field in the scrape-off layer (the magnetic mirror) has been predicted [3]. In the main plasma, a number of effects may occur [47], including (a) the enhancement of (axisymmetric) neoclassical radial fluxes, (b) the loss of high energy ions from neutral injection before slowing down, impairing neutral beam heating efficiency, and (c) the production of magnetic islands, with associated enhanced transport.

The ion temperature increases, (from charge exchange measurements), during neutral injection, are unaffected by the divertor. This shows that there is no significant increase in the loss of fast ions, or in the radial ion energy transport mechanism for a plasma in the plateau regime [see eg, Ref. [3] for definition of the different regimes]. Radial charge exchange spectra show no difference whether the divertor is on or

off, for particle energies up to 12keV. Above this energy no significant counts are recorded because of the low sensitivity of the detector.

The neutron flux, during injection of hydrogen into a deuterium plasma, is affected by less than 5% by the divertor. Without injection the flux is too low to measure accurately. Assuming a maxwellian velocity distribution, the flux during injection corresponds to a temperature of 620 ± 10eV, in reasonable agreement with that derived from the charge exchange neutral particle spectra (see Table 7). This flux originates from interacting deuterons with energies $\simeq$ 4.5keV [48], near the plasma centre where the density is highest. The constant flux thus implies no enhanced losses of plasma ions at this energy and position by the perturbed field. These ions are collisionless, in the banana regime, but passing through the magnetic mirror introduced by the poloidal and toroidal fields, rather than trapped. Because of the small number of trapped ions near the axis, little difference in neutron flux would be observed even if they were all lost. The results demonstrate no enhanced losses of collisionless, passing ions by the perturbation introduced by the divertor.

The magnetic field perturbation in the main plasma produced by the divertor fields, will affect the flux surfaces [23], and may increase the radial transport coefficients. Although this is not specifically concerned with neutral injection we include a discussion here. Field line calculations have been performed, in which the divertor fields are superimposed on the fields of an axisymmetric equilibrium configuration, and any ergodisation or magnetic island structures sought. If these are present, their radial dimension is small, $\leq$ 5mm,

for the equilibrium configurations considered. The electron energy transport has been evaluated and no difference in this value is observed whether the divertor is on or off. It is $(4 \pm 2) \times 10^3$ W m^{-2} (for 0.02m < r < 0.18m) for the conditions listed in Table 4.

All experimental evidence suggests the divertor does not increase the losses above those already present.

11 GROSS INSTABILITIES

To obtain plasma currents and densities suitable for neutral beam heating experiments, and to allow the scaling of parameters with density it has been necessary to operate with low values of safety factor, $q_s \sim 2$. Many discharges produced have exhibited characteristic instabilities, which restrict the total plasma current attainable (see Section 3). This section describes the instabilities and their effect on the performance of the divertor.

Figure 29 shows a set of results obtained with $B_\phi = 0.96$T, $I_p = 60$kA, and $\bar{n}_{eL} = 1 \times 10^{19}$ m^{-3}. The divertor is operated so that the separatrix intersects the target from 90ms after the initiation of the discharge onwards. Figure 29a shows the plasma current, and Figure 29b the plasma volts per turn. Approximately 130ms after the start, the voltage increases by ~ 30%, while the current remains constant. Figure 29c shows the line of sight average density, $\bar{n}_{eL}$, which drops, although the density control system increases the external gas flow by ≃ 20%. Both poloidal beta, β_I, measured with toroidal flux loops, and the parameter $(\beta_I + \frac{\ell i}{2})$ deduced from poloidal magnetic field measurements, remain constant, and the overall energy confinement time is reduced by ~ 30% as shown in Figure 29d. Definitions of β_I and ℓi, the internal inductance are given in [49].

Figure 30 shows in more detail, parameters measured during the period of increased voltage. Figure 30a shows the microwave interferometer signal, through a chord at r = 0; Figure 30b through a chord at r = 0.22m. Figure 30c shows the D_α (656.2nm) signal obtained by viewing the target. The large perturbations are observed on both the electron and ion drift sides. Density sawteeth are observed, similar to those associated with the growth of an instability with m = 1, n = 1 at the q = 1 surface (m,n, are the minor, major azimuthal mode numbers). Sawteeth are also seen in the impurity radiation, with the CV line (227.2nm) from the plasma core in phase with the density and the OIV line (283.6nm) from the scrape-off layer out of phase. Associated with each flattening of the density profile (the sharp break in the sawtooth) is a large increase in both D_α and TiIII (323.9nm) light from the target plate. Both indicate an increased plasma-target interaction. The D_α signal from the main torus shows a similar increase.

Also associated with the above phenomena are poloidal magnetic field oscillations, measured with 16 coils inside the vacuum vessel. Figures 30d and and 30e show the first two harmonic components $\Delta B(m=1)$ and $\Delta B(m = 2)$. Analysis of the higher harmonics is confused by the noise generated by the vertical field feedback control system. These results were not obtained on the same discharge as the results in Figures 30a to 30c, but in all cases the D_α and m=1 signals are in phase. An exponentially growing m = 2 mode (n number not measured), with a growth rate $\gamma \sim 1 \times 10^3\ s^{-1}$, is seen. An m = 1, n = 0 mode, corresponding to an inward displacement of 2mm, is also measured.

Figure 31a shows the perturbation Δf seen on the microwave interferometer phase signal f; $\Delta f/f_o$ is shown as a function of the viewing chord radius, r. An inversion at r ~ 17cm is seen. For these

discharges, the q = 2 surface is at r ~ 17cm, and the separatrix is at r_s = 17.5cm. The profiles of the perturbation to the soft X-ray signal intensity have not been obtained, because of the small signal values obtained at the low plasma densities.

In many discharges, in which the plasma current is increasing with time, an initially oscillating m = 2 mode is seen, as is usual in tokamaks, which abruptly terminates when $I_p/B_\phi \gtrsim 6 \times 10^4$ AT^{-1}, or $q_s \lesssim 2.5$. Because of the frequency response of the Fourier analysis system used with the 16 coils it is not clear if the instability has disappeared or the growth rate is too low to detect ($\lesssim 2 \times 10^2$ s^{-1}). However the presence of the density sawteeth suggests that it is still present, and that the rotation stops when the magnetic island associated with the instability overlaps the separatrix.

The following explanation is proposed to explain the phenomenon described. An m = 2, n = 1 tearing mode grows at the q = 2 surface, which is near the separatrix. If the associated magnetic island is in the scrape-off layer there is no rotation. When the island has grown so that $\Delta B_\theta/B_\theta|r = 0.29m$ is ~ 0.3%, plasma is redistributed from inside to outside the q = 2 surface, producing the observed sawteeth. It is not known why the value of 0.3% should cause the redistribution; estimates for the corresponding island width are ~ 2cm. The expulsion of plasma across the separatrix enhances the limiter and target interactions. The parameter ($\beta_I + \ell i/2$) will decrease, and the plasma move inwards in a time faster than the response time of the vertical field control system. A 2mm motion, as observed, would result from a change $\Delta(\beta_I + \ell i/2) \sim 0.07$.

Other instability phenomena have been observed. During neutral beam injection studies a sawtooth oscillation about the q = 1 surface

is usually observed. However, if beam heating is applied to a plasma which already exhibits the sawteeth about the q = 2 surface, the sawteeth whose spatial dependence is shown in Figure 30b are produced. This profile would result from the sum of two sawteeth, one at q = 1 and another at q = 2, out of phase.

We now present results of experiments to determine the effects of the instabilities at the q = 2 surface on the divertor operation.

Particle exhaust:

The current-voltage characteristics of the target and carbon limiter, biased with respect to the vacuum vessel, have been obtained. During the time when the instabilities are present, the ion current to the target increases from ~ 70A (Section 4a) to ~ 100A, while the ion current to the limiters is increased from 150A to 300A. Here the comparison is made for plasmas with the same density, $\bar{n}_{eL}$. The total particle current to all material surfaces has approximately doubled. However, the exhaust efficiency remains essentially unchanged with ξ_x ~ 0.25.

Density decay experiments show that the onset of the instabilities decreases the e-folding time. With ξ_s ~ 0.25, a confinement time at the separatrix τ_s ~ 7ms is deduced, compared to 14ms when the plasma is stable. The effect of the instabilities is to increase the time averaged outward radial transport by a factor ~ 2.

Energy exhaust:

With the instabilities present, the power to the target plates (ion and electron drift sides) is more symmetric at the lower densities. There is an increase in deposited energy, ~ 30% if the comparison is made at the same plasma density. At the same time the ohmic power

increases by ~ 30% and the temperature at the separatrix by ~ 50%. The parameter γ [equation 6] is reduced by ~ 40% at the lowest densities, suggesting that the suprathermal electrons are no longer playing such an important role.

Impurities

Figure 32 shows the intensity of the OVII line (2.16nm), for diverted discharges, both with and without the instabilities present, as a function of density, $\bar{n}_{eL}$. These results were obtained with B_ϕ = 1.44T, and $I_p \simeq$ 80kA. Comparing results at a given density, a reduction in the line intensity by ~ 35% is associated with the presence of instabilities. If the density is not kept constant, but falls by about 30% as is usually the case, a further reduction is produced. Thus the effect of the onset of the instabilities is to decrease the OVII line intensity by up to 70% (a reduction of a factor ~ 3).

An example of the effect of the instabilities on the neon line intensities, during neon injection experiments, is shown in Figure 33. This shows the average density, $\bar{n}_{eL}$, the intensity of the NeII line (369.4nm), and the intensity of the NeVIII line (77.0nm). Neon is initially present in the plasma because the walls have been loaded by previous discharges. Instabilities start at 90ms. Additional neon is added at ~ 140ms. The divertor is on throughout the discharge. At the onset of the instabilities the NeVIII line intensity shows an initial spike and then falls by a factor ~ 3, only returning to its original value when additional neon is introduced. If we take the ratio of the neon line intensities, NeII/NeVIII, to represent the ratio of the flux at the edge to the flux at the separatrix, then an increase in impurity screening, from ~ 0.2 (Figure 21) to ~ 0.5, is associated with the instabilities.

We note that, although fluctuations are present during the periods

of instability, there is an overall reduction in the impurity line intensities, and an overall increase in the ion flux to the limiters and target. The reduction in impurity lines from the centre of the plasma and increase in the outward flux, are consistent with a decrease in the confinement in the edge regions of the plasma [37]. These results suggest the use of externally applied helical fields to increase the diffusion coefficient at the edge in a controlled manner.

12 A COMPARISON OF RESULTS OBTAINED WITH THE MkIA AND MkIB DIVERTORS

Throughout this paper we have presented detailed results obtained with the MkIB divertor. Comparisons have been drawn, where suitable, with the results from the MkIA divertor. The characteristic operating conditions of the two devices are shown in Table 1. Table 8 summarises the experimental results obtained. It is obvious that the results obtained with the MkIA are better than those with the MkIB. The small differences in magnetic field parameters are insufficient to explain the differences. Some possible reasons for the discrepancies are now discussed.

Particle exhaust

Comparing values at a similar density $\bar{n}_{eL}$, a higher exhaust efficiency was derived for the MkIA. However the MkIA measurement analysis assumed a particle confinement time of 30ms and re-analysis of the results using the measured value of 14ms (Section 4) brings the two values into agreement.

Energy exhaust

A mugh higher proportion of the input power appeared at the divertor target in the MkIA than in the MkIB. At the same time, the

value of γ (equation 9) was a factor 10 higher in the MkIA. This suggests that supra-thermal electrons played a more important role in energy transport in the MkIA than the MkIB; either their energy or population density was higher.

Impurity behaviour

For low Z impurities, the screening coefficient was a factor 2 higher in the MkIA than the MkIB; for high Z impurities, a factor typically 3. One probable source of error in the measurements was in the use of line intensities and carbon probe data from the limiter regions to correct for any changes of impurity source in the MkIA. Measured asymmetries imply that these results were not necessarily representative of the total input.

Line intensities from intrinsic impurities in the region $r < a_s$ were reduced more by the MkIA than the MkIB divertor. For low Z impurities the reduction was a factor 2 greater in the MkIA than in the MkIB, for high Z impurities a factor $\gtrsim 5$. Although large reductions are predicted by the model of impurity production for the condition applicable to the MkIA device (see Section 9 and Table 6), the measured reductions are greater than expected. One possible explanation for this, and also for the different screening efficiencies, is related to the instability phenomena described in Section 11. For whatever reason, these instabilities are accompanied by a reduction in the oxygen line intensity of a factor 2-3, (Figure 32), and an increase in the screening of neon of a factor ~ 2.5 (Figure 33).

The diagnostics used to identify the instability behaviour on the MkIB were not always available on the MkIA. However a re-assessment of MkIA results, in particular the perturbations to plasma voltage and position, suggests that the instabilities were present in many

discharges, including those used to obtain the impurity line radiation intensities.

The larger population, or higher energy, of the supra-thermal electrons present with the MkIA may also play a role in explaining the impurity line intensities. Operating the MkIA divertor removes the interaction between these supra-thermal electrons and a material surface from the limiters to the target. If this supra-thermal electron limiter interaction is a source of impurities, then operating the divertor would result in a reduced influx of heavy impurities into the plasma. This could explain the large reduction observed in molybdenum line intensities, up to a factor of 50, with the MkIA.

The difference between the MkIA and MkIB divertors in reducing the radiated power reflects their different effects on the impurities, in particular the heavy metals. The values of Z_{eff} are almost unchanged in both cases, consistent with the major contribution coming from oxygen: there is only a small change in the oxygen line intensities if the plasma density is carefully controlled.

13 A COMPARISON OF RESULTS OBTAINED WITH THE BUNDLE DIVERTOR, AND OTHER DIVERTORS

Although this paper is specifically concerned with describing the results of experiments on the bundle divertor, it is useful to compare the DITE results with those from other tokamaks fitted with divertors. An abbreviated list of parameters obtained is shown in Table 9. All divertors, except for DITE, are poloidal. In Doublet III there is no specific target chamber. A large parameter range is represented: for example I_p varies from 40kA (T12, DIVA) to 500kA (Doublet). The values quoted are meant to be representative of those obtained over a variety

of conditions. For DITE, values from the MkIB divertor, with stable discharges, are shown.

If we consider the main objectives of a divertor to be exhaust and impurity reduction, then the DITE results are not as good as the others. The bundle divertor is less efficient in particle and energy exhaust than poloidal divertors. A detailed comparison is complicated by the different operating conditions of the machines. The flow to a bundle divertor [equation 5] is determined by the magnetic mirror ratio and $\bar{q}_D$; typically 4 and 7, respectively. In a poloidal divertor these are ~ 1 and ~ 3. Bundle divertor design should concentrate on the reduction of these two parameters, at the same time ensuring that any perturbed fields do not enhance ion losses. These improvements can be brought about by a hybrid poloidal-bundle divertor [32,50]. Preliminary calculations show that, using only the space between one pair of toroidal field coils, values $\bar{q}_D \sim 5$, and $M \sim 1$ can be achieved.

In the case of the bundle divertor, at the higher densities used, the particle and energy exhaust are consistent with a model for the parallel flow to the divertor which includes sheath effects, an ionisation model, and a diffusion coefficient $D_\perp = k/n_e$, with $k \sim 3 \times 10^{18}$ $m^{-1}\ s^{-1}$. When this diffusion coefficient becomes larger than the Bohm value, for example outside the limiter, $D_\perp \sim D_{BOHM}$ predicts the correct density behaviour. However, in the case of poloidal divertors, a diffusion coefficient $D_\perp \sim 0.1 \times D_{BOHM}$ is consistent with the experimental results [51,54]. Such a diffusion coefficient is not capable of explaining the DITE results, firstly because it is typically a factor 4 too small, and secondly because it decreases, rather than increases with increasing radius across the separatrix. Without a detailed knowledge of the parametric dependence of $D_\perp$ it is impossible to extrapolate

the results presented in this paper to other conditions. However, the experimental scaling of both particle exhaust and impurity screening shows improved efficiencies with increasing densities, which omens well for future bundle divertor operation.

14 CONCLUSIONS

a) Magnetic Limiter

The separatrix position determines the plasma current and density which can be obtained, in a similar manner to a limiter. Part of the plasma-limiter interaction is removed to the target. The safety factor at the separatrix controls the plasma current: for stable discharges $q_s \gtrsim 2$.

b) Particle Exhaust

30% of the outward ion flux flows to the divertor target. This value increases with increasing density. The parallel flow velocity is ~ 0.4 times the sound speed. The resulting electron density profiles in the scrape-off layer can be reproduced by a model which includes molecular ionisation, the effect of magnetic geometry on the parallel ion loss, and a radial diffusion coefficient $D_\perp = k/n_e$, $k \sim 2.5.10^{18}$ m^{-1} s^{-1}.

c) Energy Exhaust

Approximately 15% of the conducted and convected energy appears at the target plate. This is consistent with a model for the parallel ion loss, and an electrostatic sheath at the target. At low densities, supra-thermal electrons may transport energy to the target.

d) Impurity Screening

The divertor reduces the impurity influx from the edge to the central regions of the plasma by 35%; this value increases with density. To explain this result, the impurity ions must have an inward diffusion velocity $\simeq 50 ms^{-1}$.

e) Particle Retention

Measurements suggest that less than 30% of the plasma entering the target chamber returns to the main torus.

f) Overall Impurity Reduction

Only small reductions in line intensities, radiated power and resistance anomaly are observed, typically 30%. The small reductions are consistent with the charge exchange neutral flux producing the impurities, and the measured exhaust and screening efficiencies. However, no direct experimental evidence exists to show which impurity source term is dominant.

g) Neutral Injection

All experimental evidence shows that the bundle divertor does not adversely effect the ion confinement.

h) Instabilities

With the safety factor at the limiter $\lesssim 2$, gross instabilities affect the divertor operation. In particular they increase the ion flux to the limiters, and reduce the impurity radiation from the main plasma. The overall energy and particle confinement time is reduced.

i) MkIA and MkIB Operation

The MkIA divertor was, under some circumstances, more efficient than the MkIB. This was probably due to a higher proportion of supra-thermal electrons, and the presence of gross instabilities.

j) The Bundle Divertor Compared with Poloidal Divertors

At the present time the DITE bundle divertor is less efficient than existing poloidal divertors. Extrapolation to different plasma parameters and larger machines cannot be made without a knowledge of the parametric dependence of the relevant transport coefficients. This requires further experiments.

ACKNOWLEDGEMENTS

We wish to thank the DITE operating team for their invaluable assistance in the experimental work and Drs. R. Bickerton and D. Sweetman for their advice and encouragement.

TABLE 1

Parameters and characteristic conditions

Divertor	MkIA	MkIB	
Toroidal field B_ϕ (T)	0.9	0.96	1.44
Major radius R (m)	1.17	1.17	1.17
Limiter material	Molybdenum	Titanium	Titanium
Limiter minor radius a_L (m)	0.27	0.26	0.26
Separatrix minor radius a_s (m)	0.16	0.175	0.175
Mirror ratio (M)	4	3.6	3.6
Mean number of field line transits around torus per transit of divertor, $\bar{q}_D$	6.5	7.4	7.4
Usual working gas	Hydrogen	Deuterium	Deuterium
Usual vacuum vessel wall condition	Stainless steel	Stainless steel covered by titanium	Stainless steel covered by titanium
Plasma current I_p (kA)	45	55	85
Line of sight average density $\bar{n}_{eL}$ (m^{-3})	6×10^{18}	1.2×10^{19}	2×10^{19}
Central electron temperature T_e (O) (eV)	300	450	550

TABLE 2

Particle fluxes; $\bar{n}_{eL} = 1.2 \times 10^{19}$ m^{-3} (MkIB, in deuterium)

	Divertor off	Divertor on
Limiters	220A	150A
Target	0	70A

Exhaust efficiency $\xi_x \sim 0.3$, increasing with density

Diffusion coefficient $D_\perp \sim \frac{2.5}{n_e (m^{-3})} \times 10^{18}$ m^2 s^{-1}

TABLE 3

Energy exhaust, (MkIB, in deuterium)

density, $\bar{n}_{eL}(m^{-3})$	3×10^{18}	6×10^{18}	1.2×10^{19}
particle energy (eV)	4000	500	150
γ	150	20	6

TABLE 4

Measured and deduced plasma parameters

with and without the MkIB divertor, using deutium

	Gettered		Non-Gettered	
Parameter	Divertor on SN912933 to 60	Divertor off SN913017 to 37	Divertor on SN014078 to 95	Divertor off SN015364 to 85
I_p (kA)	60	68.5	55.7	54.2
V_p	1.4	1.5	2.1	2.3
B_ϕ (T)	0.924	0.921	0.925	0.938
q(limiter)	4.45	3.9	4.8	5.0
q(o) (from T_e(r))	0.9	0.7	0.83	0.78
T_e(o) eV	450	450	430	470
T_i(o) eV	158	145	158	158
n_e(o) (m^{-3})	2.1×10^{19}	2.2×10^{19}	2.2×10^{19}	2.1×10^{19}
T_e(0.17m) (eV)	90	80	85	97
n_e(0.17m) (m^{-3})	6.5×10^{18}	6.5×10^{18}	8.8×10^{18}	8.5×10^{18}
β_I	0.5	0.4	0.6	0.6
PΩ (kW)	84	103	117	124
P_{RAD} (kW)	32	60	108	111
P_{TARGET} (kW)	8	0	~ 8	0
Z_{eff}	1.4	1.4	2.7	3.1
A_x X-ray	4	20	10	40
τ_{Ee}(0.17m) (ms)	12	9	7	6
τ_{Ei}(0.17m) (ms)	14	18	14	15
I OVII (a.u)	0.25	0.25	1.0	1.0
I TiXIV (a.u)		0.44	0.71	1.0
I CV (a.u)			0.72	1.0
I CIV (a.u)			0.9	1.0

TABLE 5

Coefficients used in the global model for impurity production

Desorption yields [41]

Low Z by D^+ : $y^i = 2 \times 10^{-3}$

Low Z by neutrals : $y^o = 5 \times 10^{-3}$

D by neutrals : $y^n = 0.1$

Sputtering yields [42]

High Z by D^+ : $S^i = 3 \times 10^{-4}$

High Z by neutrals : $S^o = 3 \times 10^{-3}$

High Z by low Z : $S^L = 2 \times 10^{-2}$ for charge state 1, 0.2 for charge state 4

High Z by high Z : $S^H = 3.5 \times 10^{-2}$ for charge state 1, 0.35 for charge state 4

Energies

Sheath potential = 50eV (experimental)

Charge exchange neutral energy = 100eV (assumed)

Confinement Times

D^+ : τ_i = 15ms (experimental)

impurities : $\tau_L = \tau_H$ = 15ms (assumed)

Shielding coefficients

D^+ : ξ_s^i = 0.8 divertor on, 0 divertor off (experimental)

Low Z : ξ_s^L = 0.3 divertor on, 0 divertor off (experimental)

High Z : ξ_s^H = 0.3 divertor on, 0 divertor off (experimental)

Exhaust coefficients

D^+ : ξ_x^i = 0.3 divertor on, 0 divertor off, (experimental)

Low Z : ξ_x^L = 0.3 divertor on, 0 divertor off, (assumed)

High Z : ξ_x^H = 0.3 divertor on, 0 divertor off, (assumed)

Wall concentrations

D : 10^{19} m^{-2} (assumed)

Reflection coefficients [11]

Fast neutrals : $\beta = 0.5$

Ions, returning as fast neutrals : $\beta = 0.5$

TABLE 6

A summary of experimental and predicted impurity fluxes

Values quoted represent the ratio of fluxes into the main plasma, divertor on to divertor off. Experimental results refer to line intensity ratios.

MkIB	Experiment	Model
Low Z	Oxygen 1.0 Carbon 0.7	0.7 0.7
High Z	Titanium 0.7	0.7

MkIA	Experiment	Model
Low Z	Oxygen ~ 0.5 Carbon ~ 0.5	~ 0.7 ~ 0.7
High Z wall material	Iron 0.1 to 0.3	~ 0.7
High Z limiter material	Molybdenum 0.02 to 0.05	~ 0.3 to 0.5

TABLE 7

Neutral injection heating

(400kW neutral injection)

a) $\bar{n}_{eL} = 1.2 \times 10^{19}\ m^{-3}$, $B_\phi = 0.96T$ (from 9/79)

	Divertor off	Divertor on
$T_e(o)$ (eV)	From 450 to 450	From 450 to 450
$T_i(o)$ (eV)	From 150 to 300	From 150 to 280

b) $\bar{n}_{eL} = 2 \times 10^{19}\ m^{-3}$, $B = 1.44T$ (from 5 and 6/80)

	Divertor off	Divertor on
$T_e(o)$ (eV)	From 600 to 770	From 550 to 740
$T_i(o)$ (eV)	From 280 to 570	From 250 to 550

TABLE 8

A summary of experimental results

Parameter	MkIA	MkIB	
Density, $\bar{n}_{eL}$ (m^{-3})	~ 7 x 10^{18}	(6-8) x 10^{18}	1.2 x 10^{19}
Particle exhaust: the fraction of the particle outflux at the separatrix reaching the divertor	0.3 [10]	0.15	0.3
Energy exhaust: the fraction of the conducted and convected power reaching the divertor	0.8[5,7,8,10]	0.15	0.15
Impurity screening: the fraction of incoming impurity flux reaching the divertor — low Z :	0.5 [8,10]	0.25	0.35
high Z :	0.75 to 0.8 [8,10]	0.25	0.35
Impurity line radiation from r < a_s, divertor on/ divertor off — low Z :	0.2 to 0.7 [6,7,12]	0.7 to 1.0	0.7 to 1.0
high Z :	0.02 to 0.3 [6,7,8]		0.7
Radiated power, divertor on/divertor off	0.13 to 0.5 [5,7,8,12]	0.7 to 1.0	0.7 to 1.0
Z_{eff}, divertor on/ divertor off	0.75 to 1.0 [5,6,7,8,10]		0.85 to 1.0

TABLE 9

Experimental Divertor Results

PARAMETER	DITE	DIVA[51]	PDX[52]	ASDEX[53]	T12[54]	DOUBLET III[55]
Particle exhaust	0.3	0.33	-	-	1	-
Energy exhaust	0.15	0.75	1	> 0.2	1	> 0.3
Impurity screening	Ne,Al,A : 0.35	C : 0.5 Al : 0.7	Si 0 to 0.9	-	-	A : 0.6
Impurity reduction divertor on/divertor off	O : 1.0 C : 0.7 Ti : 0.7	O,C,Au : 0.25 to 0.5	O : 0.3 Ti : 0.2	O : 1.4 Fe : 0.05	C,O : 0.6	Ni : 0.1
Fraction of radiated power, divertor on/divertor off	0.7 to 1	0.25 to 0.5	0.4 to 0.75	0.6	0.5	0.6
Z_{eff}, divertor on/divertor off	0.85 to 1	0.6	0.5	-	-	0.6

REFERENCES

1. Colven, C.M., Gibson, A., Stott, P.E., in Controlled Fusion and Plasma Physics, (Proc. 5th European Conference, Grenoble, 1972).

2. Stott, P.E., Wilson, C.M., Gibson, A., Nucl. Fus. 17, 481 (1977).

3. Stott, P.E., Wilson, C.M., Gibson, A., Nucl. Fus. 18, 475 (1978).

4. Plummer, K.M. et al., Proc. 6th Symposium on Engineering Problems of Fusion Research, 361 (1975).

5. Paul, J.W.M., Axon, K.B., Burt, J., Craig, A.D., Erents, S.K., Fielding, S.J., Gill, R.D., Goodall, D.H.J., Hemsworth, R.S., Hobby, M., Hugill, J., McCracken, G.M., Pospieszczyk, A., Powell, B.A., Prentice, R., Reid, G.W., Stott, P.E., Summers, D.D.R., Wilson, C.M., 6th IAEA Conference on Plasma Physics and Controlled Nuclear Fusion Research, Bertchesgaden, Paper IAEA-CN-35/A17, (1976), 2, IAEA Vienna (1977), 269.

6. Peacock, N.J. et al., 7th IAEA Conference on Plasma Physics and Controlled Nuclear Fusion Research, Innsbruck, Paper IAEA-CN-37/N-5-2(B), (1978).

7. Stott, P.E., Burt, J., Erents, S.K., Fielding, S.J., Goodall, D.H.J., Hobby, M., Hugill, J., McCracken, G.M., Paul, J.W.M., Pospieszczyk, A., Prentice, R., Summers, D.D.R., Proc. Symp. on Plasma Wall Interactions, Julich, 39, (1976). (CLM-P473).

8. Fielding, S.J., Hobby, M., Hugill, J., McCracken, G.M., Paul, J.W.M., Peacock, N.J., Powell, B.A., Stott, P.E., 8th European Conference on Controlled Fusion and Plasma Physics, Prague, 1, 36, (1977).

9. McCracken, G.M. et al., 8th European Conference on Controlled Fusion and Plasma Physics, Prague, 1, 40, (1977).

10. Stott, P.E., Fielding, S.J., McCracken, G.M., Paul, J.W.M., Journal of Nuclear Material, 76 & 77, 528, (1978).

11. Fielding, S.J., McCracken, G.M., Stott, P.E., Journal of Nuclear Materials, 76 & 77, 273, (1978).

12. Fielding, S.J., Paul, J.W.M., Wootton, A.J., 9th European Conference on Controlled Fusion and Plasma Physics, Oxford, Paper EP8, (1979).

13. Fielding, S.J. and Wootton, A.J., 4th International Conference on Plasma Surface Interactions in Controlled Fusion Devices, Garmisch-Partenkirchen, Paper D3, (1980). J. Nucl. Mat., 93 & 94, 226 (1980).

14. Erents, S.K., Hotson, E., McCracken, G.M., Sofield, C.J., Shea, J., 4th International Conference on Plasma Surface Interactions in Controlled Fusion Devices, Garmisch-Partenkirchen, Paper A2, (1980). J. Nucl. Mat., 93 & 94, 115 (1980).

15. Fielding, S.J., Sanderson, A.D., 4th International Conference on Plasma Surface Interactions in Controlled Fusion Devices, Garmisch-Partenkirchen, Paper D2, (1980). J. Nucl. Mat. 93 & 94, 220 (1980).

16. Proudfoot, G., Harbour, P.J., 4th International Conference on Plasma Surface Interactions in Controlled Fusion Devices, Garmisch-Partenkirchen, Paper J2, (1980). J. Nucl. Mat. 93 & 94, 413 (1981).

17. Goodall, D.H.J., Proc. of the International Symposium on Plasma Wall Interactions, Julich, 53, (1976).

18. Axon, K.B., et al., 8th International Conference on Plasma Physics and Controlled Nuclear Fusion Research, Brussels, Paper IAEA-CN-38/X3, (1980).

19. Fielding, S.J., Wootton, A.J., Physica Scripta, 23, 97 (1981).

20. Paul, J.W.M., et al., in Proc. of the 6th International Conference on Plasma Physics and Controlled Nuclear Fusion Research, Berchtesgaden, West Germany, 1976, Vol 2, P269.

21. Paul, J.W.M., et al., 8th European Conference on Controlled Fusion and Plasma Physics, Prague, invited paper, (1977).

22. Fielding, S.J., Hugill, J., McCracken, G.M., Paul, J.W.M., Prentice, R., Stott, P.E., Nucl. Fus., 17, 1382 (1977).

23. Taylor, J.B., Culham Report, R132, (1974).

24. Hugill, J., Wootton, A.J., Axon, K.B., Powell, B.A., Prentice, R., Summers, D.D.R., Wilson, C.M., 9th European Conference on Controlled Fusion and Plasma Physics, Paper EP11, Oxford (1979).

25. Kimura, H., et al., Nucl. Fus., 18, 1195 (1978).

26. Jeans, J., in An Introduction to the Kinetic Theory of Gases, Cambridge, (1940).

27. Ando, K., et al., 5th IAEA Conference on Plasma Physics and Controlled Nuclear Fusion Research, Tokyo, Paper IAEA-CN-33/B4-4, (1975).

28. Kimura, H., et al., JAERI Report, JAERI-M 6861 and 6971, (1977).

29. Callen, J.D., et al., 8th International Conference on Plasma Physics and Controlled Nuclear Fusion Research, Brussels, Paper IAEA-CN-38/Y3, (1980).

30. Emmert, G.A., University of Wisconsin Report, UWFDM-343, (1980).

31. Erents, S.K., McCracken, G.M., Vince, J., Journal of Nuclear Materials, 76 & 77, 623 (1978).

32. INTOR Report, EUR FU BRU/XII 501/79/EDV 50, (1979), and international Tokamak Reactor, Zero Phase, IAEA, Vienna (1979).

33. Harbour, P.J., Harrison, M.F.A., Journal of Nuclear Materials, 76 and 77, (1978), 513.

Harbour, P.J., Harrison, M.F.A., Nucl. Fus, 19, (1979), 785.

34. Knopefel, H., Spong, D.A., Nucl. Fus., 19, (1979), 785.

35. Marmar, E.S., Cecchi, J.L., Cohen, S.A., Rev. Sci, Inst., 46, 1149, (1975).

36. Isler, R.C., Crume, E.C., Howe, H.C., Nucl. Fus., 19, 727, (1979).

37. Engelhardt, W., Feneberg, W., Journal of Nuclear Materials, 76 and 77, 518, (1978).

38. Rutherford, P.H., et al., Proc. of the International Symposium on Plasma Wall Interactions, Julich, 173, (1976).

39. McCracken, G.M., private communication, (1980).

40. Gill, R.D., Axon, K.B., Paul, J.W.M., Prentice, R., Nucl. Fus., 19, 1003, (1979).

41. Staib, P., Staudenmaier, G., Journal of Nuclear Materials, 76 and 77, 78, (1978).

42. Nishi, M., et al., Princeton Report, PPPL-1521, (1979).

43. Staudenmaier, G., Staib, P., Poschenrieder, W., J. Nucl. Mat., 93 and 94, 121, (1980).

44. Sofield, C.J., McCracken, G.M., Bridwell, L.B., Shea, J., Hotston, E.S., Erents, S.K., Nucl. Instrum. and Method, (1981), to be published.

45. Goodall, D.H.J., Journal of Nuclear Materials, 93 and 94, 154, (1980).

46. Clark, W.H.M., et al., Nucl. Fus., 22, 333, (1982).

47. Isler, R.S., et al., 8th International Conference on Plasma Physics and Controlled Nuclear Fusion Research, Brussels, 1980, paper IAEA-CN-38/A-5.

48. Gill, R.D., in Plasma Physics and Nuclear Fusion Research, (ed. R.D. Gill), (1981), Academic Press.

49. Shafranov, V.C., Plasma Physics, 13, 757, (1971).

50. Furth, H.P., Ludescher, C., Yang, T., USA Report to INTOR, Group 3, 'Impurity Control', 1979.

51. DIVA Group, Nucl. Fus., 18, 1619, (1978).

52. Maede, D., et al., 8th International Conference on Plasma Physics and Controlled Nuclear Fusion Research, Brussels, 1980, Paper IAEA-CN-38/X-1.

53. Keilhacker, M., et al., Ibid.

54. Bortnikov, A.V., et al., 7th International Conference on Plasma Physics and Controlled Nuclear Fusion Research, Innsbruck (1978), Paper IAEA-CN-37/T-3-2.

55. Nagami, M., et al., 8th International Conference on Plasma Physics and Controlled Nuclear Fusion Research, Brussels, (1980).

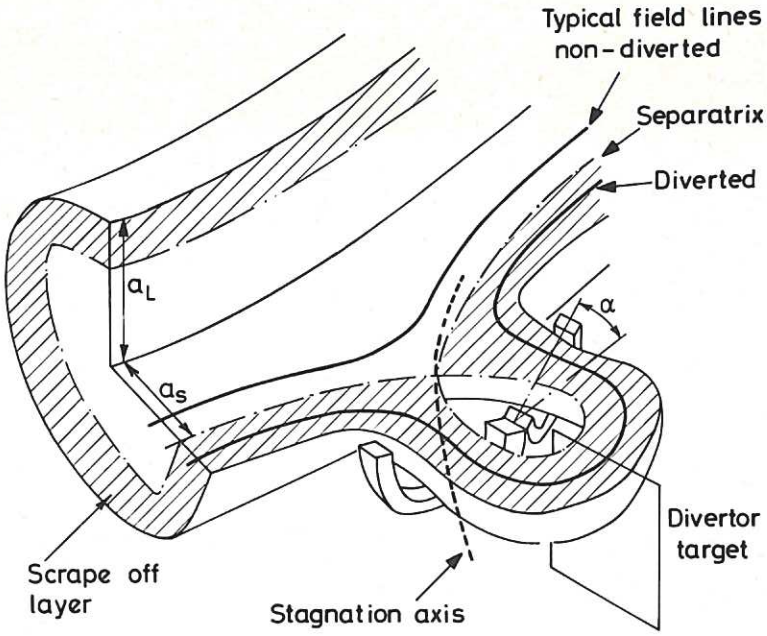

Fig.1 A schematic diagram of the bundle divertor.

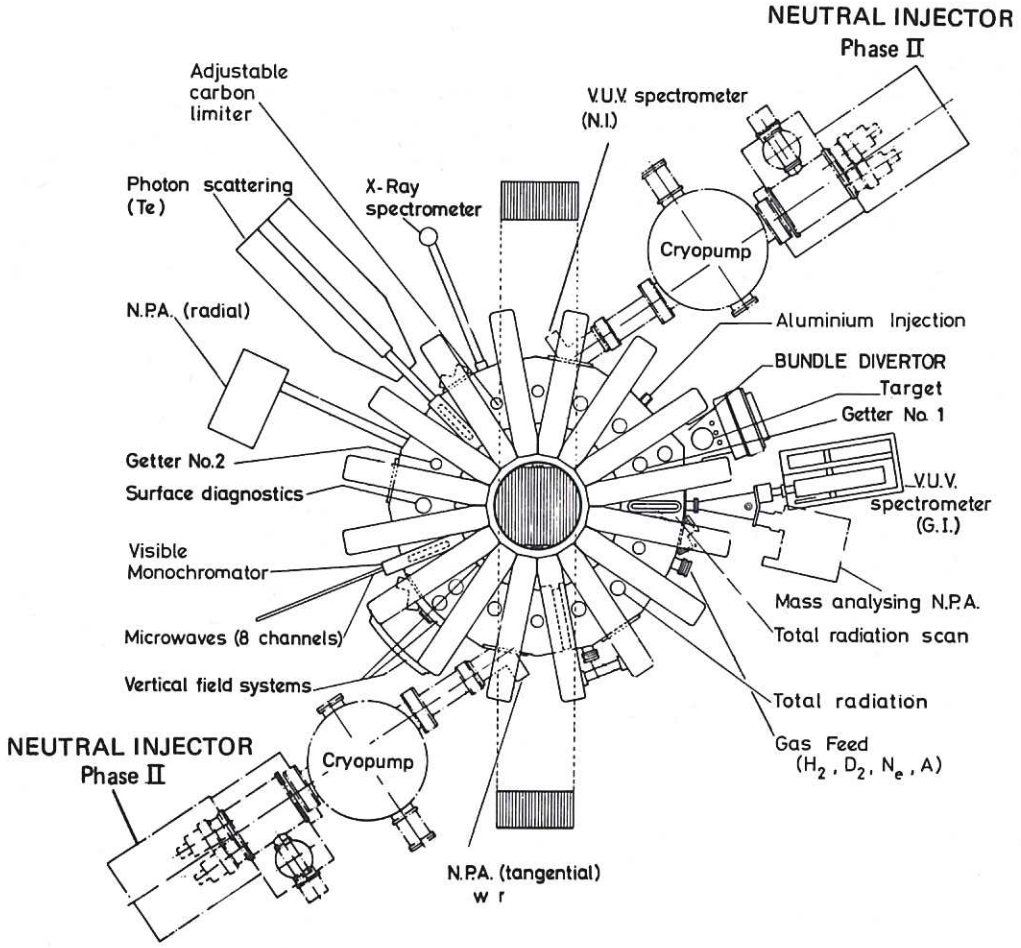

Fig.2 A plan view of DITE, showing the relative positions of the diagnostics, divertor and neutral injection beam lines.

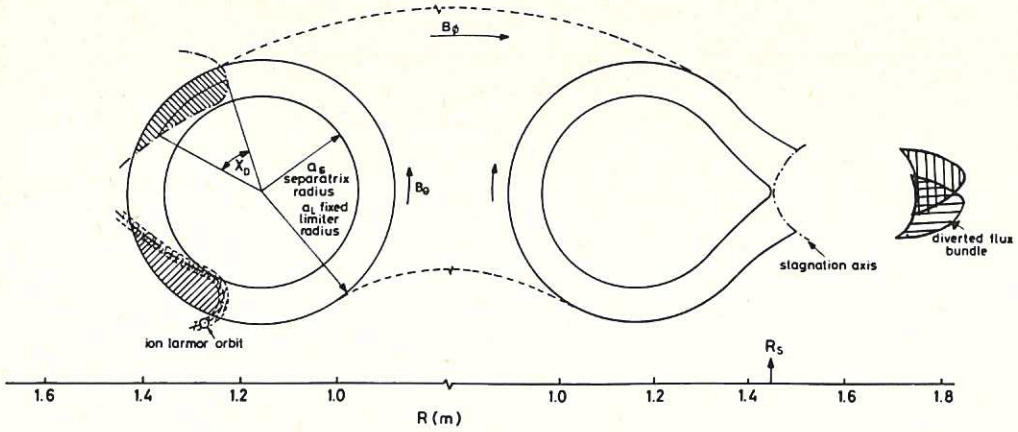

Fig.3 Boundaries of the scrape-off layer and diverted flux bundle, in the plane of symmetry of the divertor.

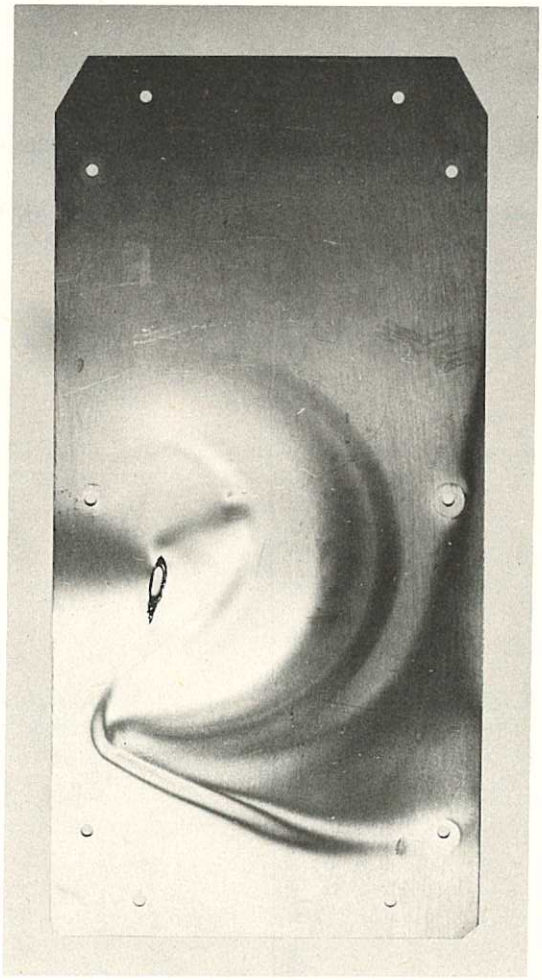

Fig.4 A molybdenum target plate, after use in low density discharges (MkIA).

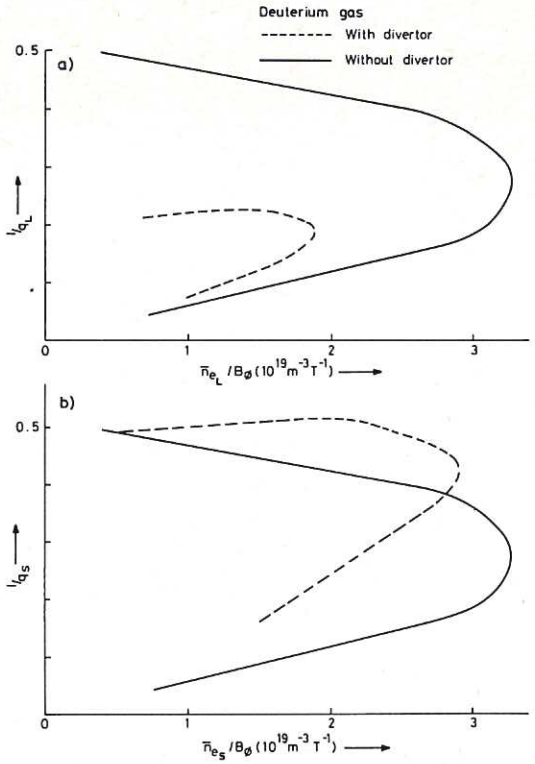

Fig.5 (a) The boundaries in $1/q_L$, $\bar{n}_{eL}/B_\phi$) space within which stable discharges can be achieved (MkIB).
(b) The boundaries in ($1/q_s$, $\bar{n}_{es}/B_\phi$) space within which stable discharges can be achieved (MkIB).

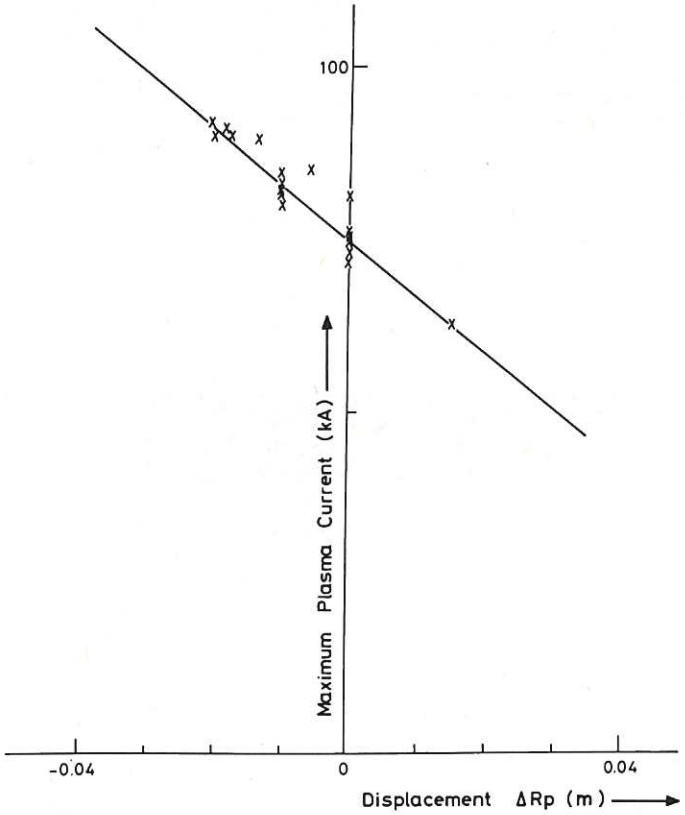

Fig.6 The maximum plasma current I_p obtainable with stable discharges, for different plasma column positions. The line is a straight line fit to the experimental points (from 5 and 6/80, MkIB).

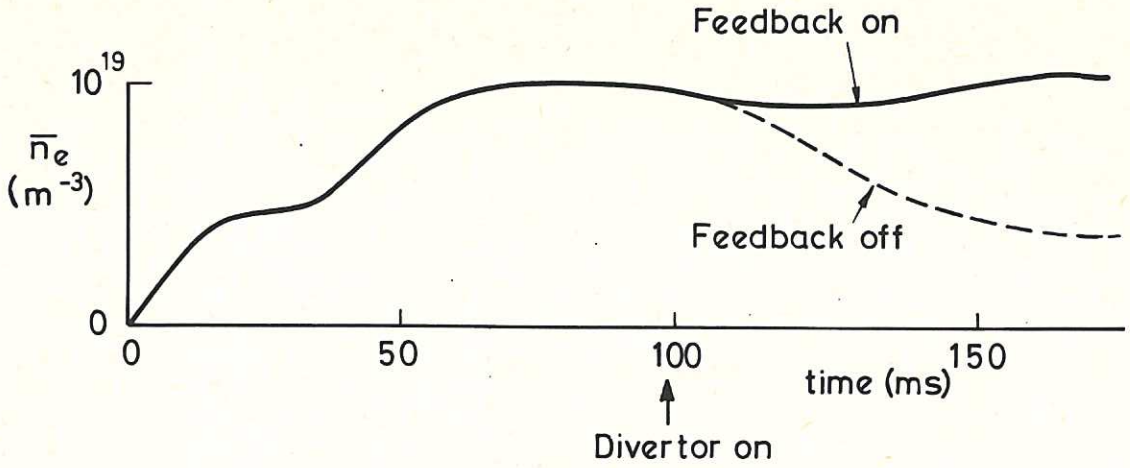

Fig.7 The plasma density, $\bar{n}_{eL}$, with and without the additional gas flow provided by a feedback system (MkIB, not gettered). The divertor is switched on mid-pulse.

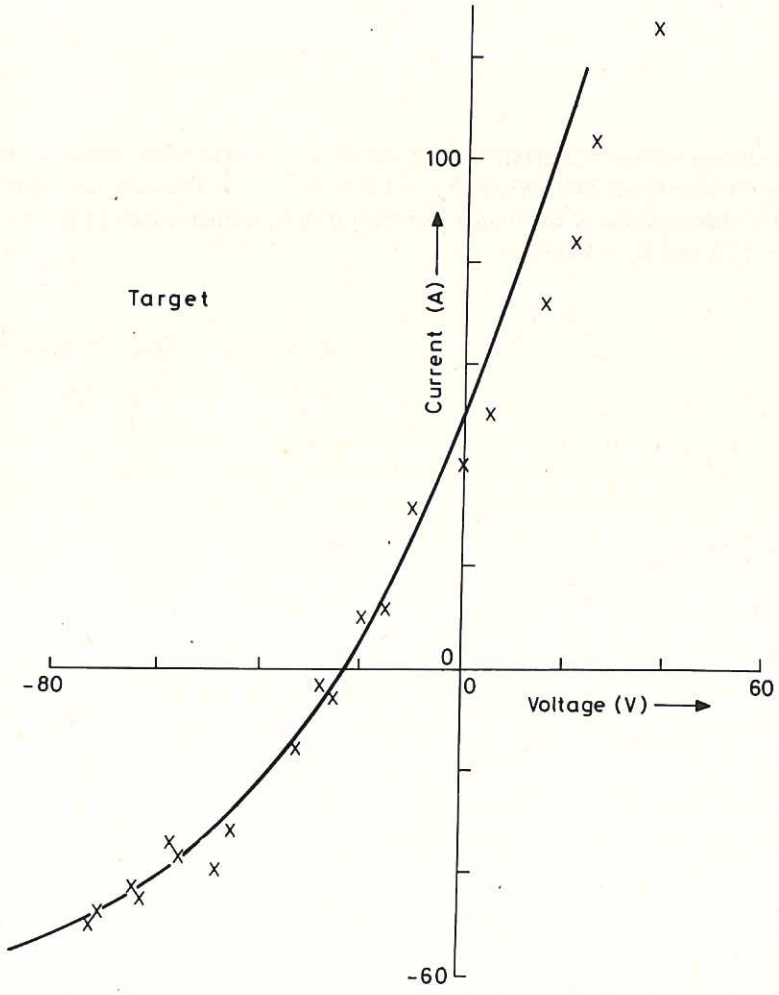

Fig.8 The current-voltage characteristic of the target plate (from 5/80 MkIB, $\bar{n}_{eL} = 1.2 \times 10^{19}\ m^{-3}$). The solid line represents the calculated I-V characteristic of the target plate assuming it to be a single plane Langmuir probe with a saturated ion current of 70A. The value of T_e estimated from the data with these assumptions is $T_e \sim 42eV$.

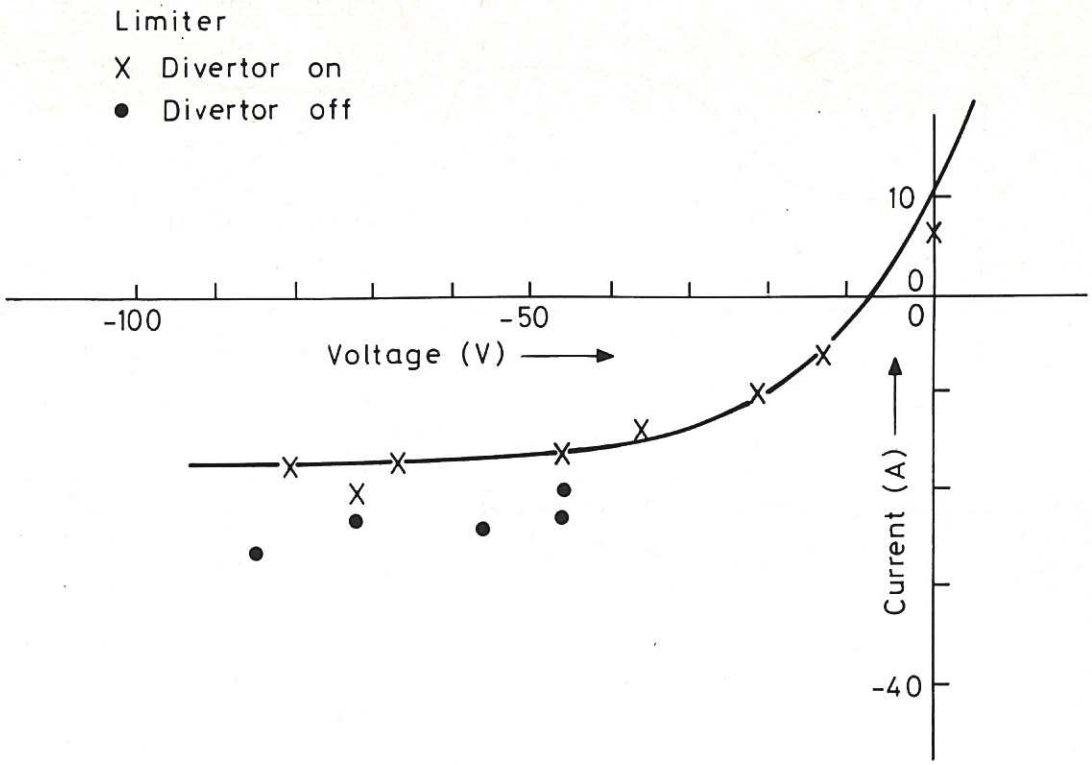

Fig.9 The current-voltage characteristic of a carbon limiter in the main torus, with and without the divertor (from 5/80, MkIB, $\bar{n}_{eL} = 1.2 \times 10^{19}$ m^{-3}). The solid line represents the fitted I-V characteristic of the limiter assuming it to be a single plane Langmuir probe giving $I_{sat} \sim 17$A and $T_e \sim 14$eV.

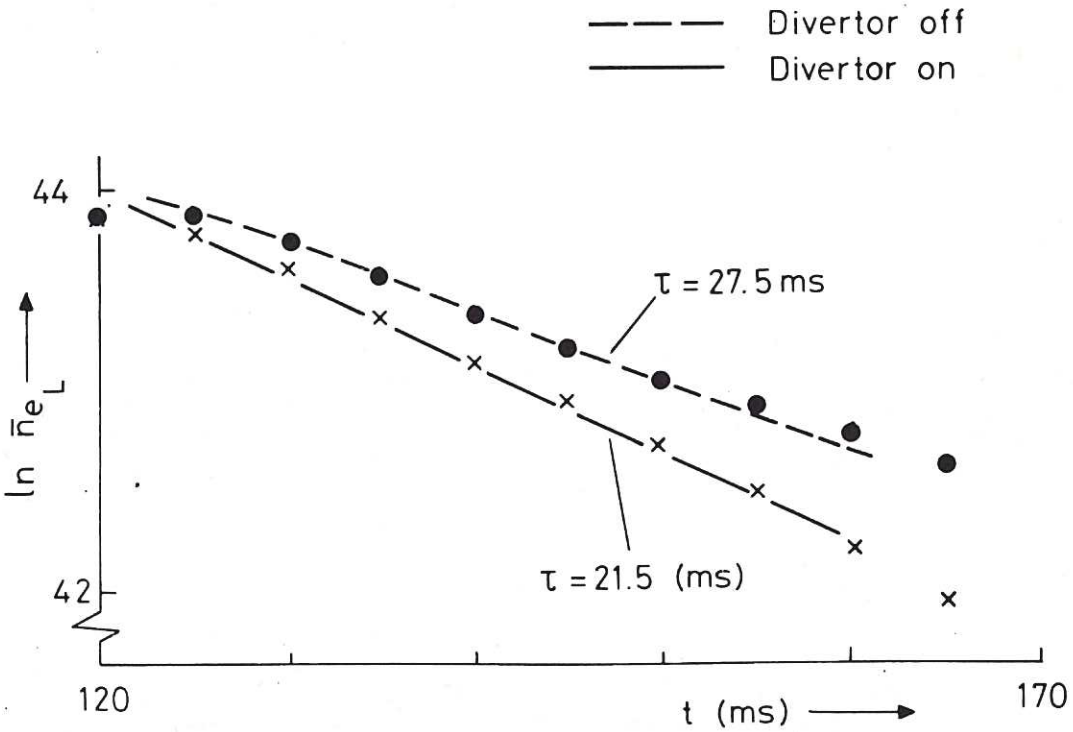

Fig.10 The value of ℓn ($\bar{n}_{eL}$) VS time during a density decay experiment, with and without divertor. The density e-folding times are shown (from 3/3/80, MkIB, $\bar{n}_{eL} = 1.2 \times 10^{19}$ m^{-3}).

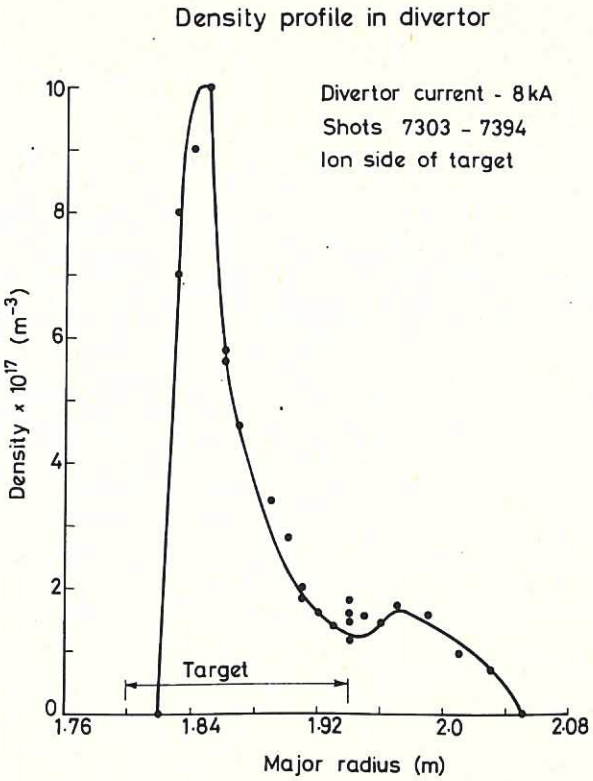

Fig.11 The density profile in front of the target plate, (mkIA, $\bar{n}_{eL} \simeq 7 \times 10^{18}\ m^{-3}$).

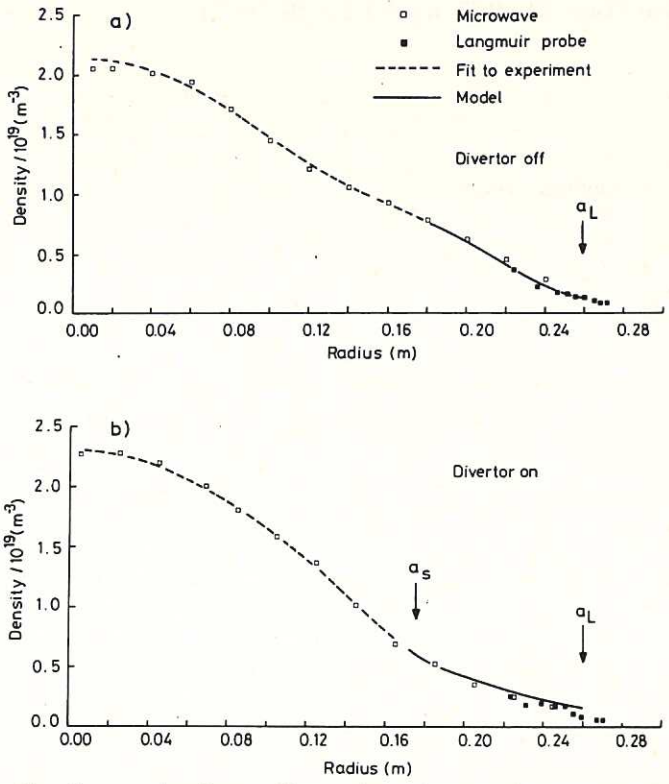

Fig.12 (a) The electron density profile, without divertor (from SN913017 to 37).
(b) The electron density profile, with divertor (from SN912933 to 60), (MkIB, $\bar{n}_{eL} = 1.2 \times 10^{19}\ m^{-3}$). The solid lines represent the predictions of a model. The broken lines represent a cubic spline fit to the data points.

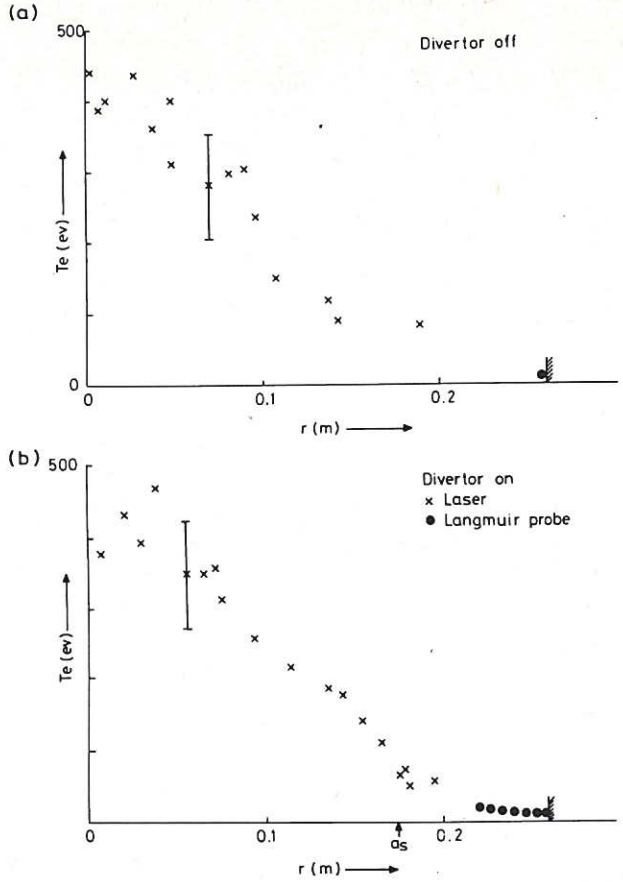

Fig.13 The electron temperature profile, with and without divertor (SN as Figure 12, MkIB, $\bar{n}_{eL} = 1.2 \times 10^{19}\ m^{-3}$).

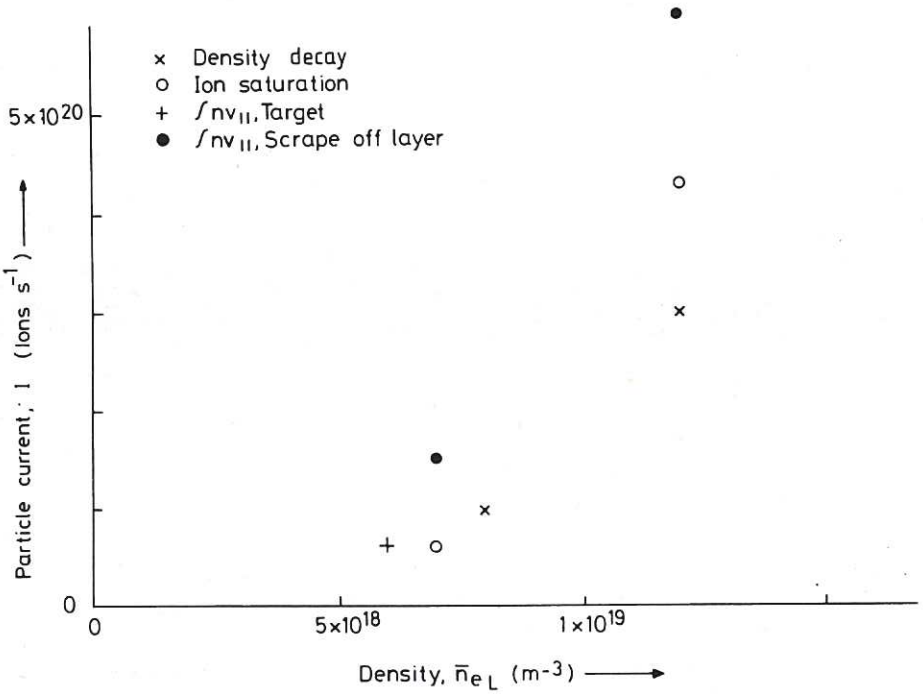

Fig.14 The particle current to the divertor, I_D, as a function of the density, $\bar{n}_{eL}$, obtained by four different experimental techniques.

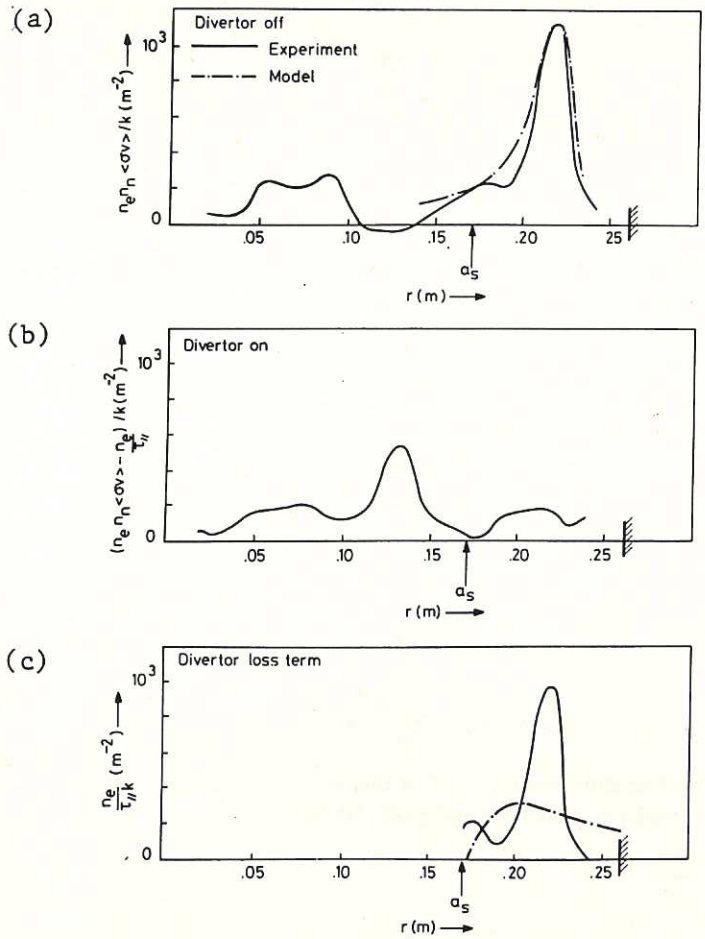

Fig.15 (a) Particle source term from ionisation, no divertor
(b) Particle source term plus parallel loss term, with divertor
(c) Particle loss term (to the divertor). The solid lines are derived from the electron density profiles, the broken lines from model calculations (MkIB, $\bar{n}_{eL} = 1.2 \times 10^{19}\ m^{-3}$).

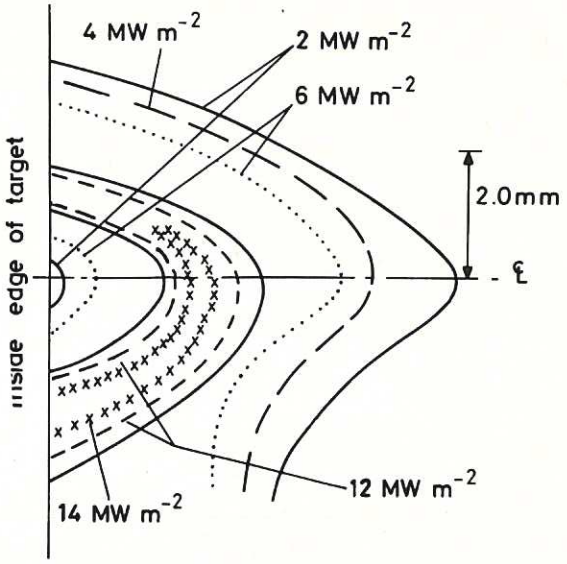

Fig.16 Contours of power deposited on the electron drift side of the target plate (MkIA, $\bar{n}_{eL} \sim 6 \times 10^{18}\ m^{-3}$).

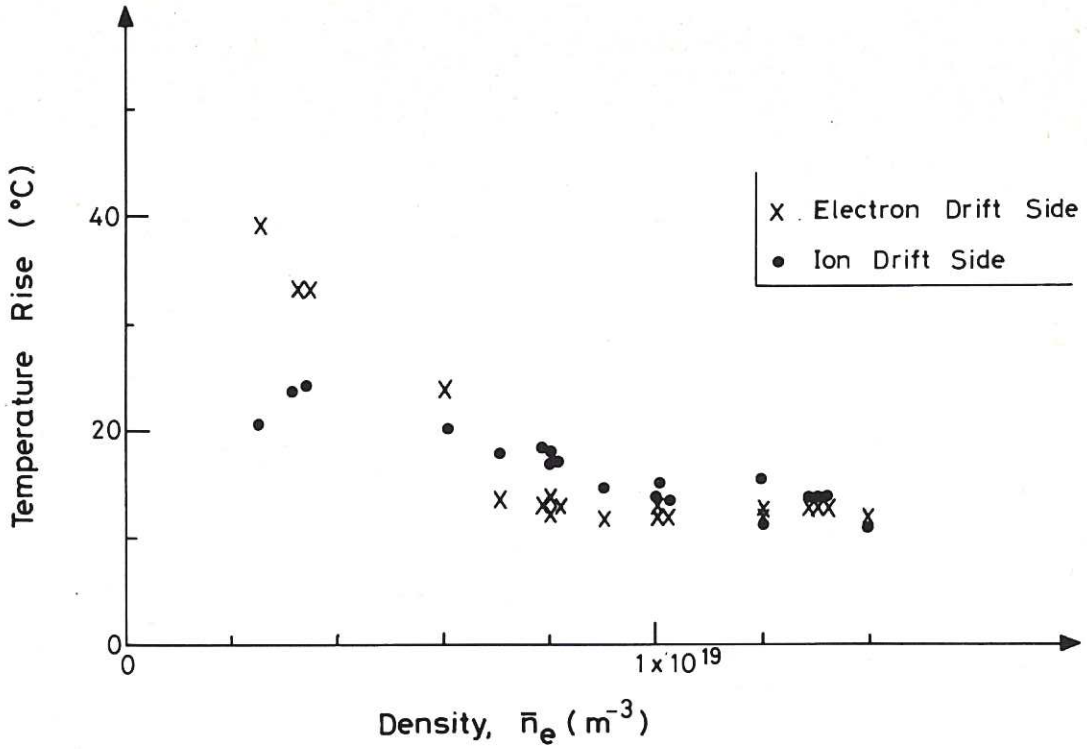

Fig.17 The maximum temperature rise recorded at the back of the target, electron and ion drift sides, as a function of average density $\bar{n}_{eL}$ (from 4 and 5/80, MkIB).

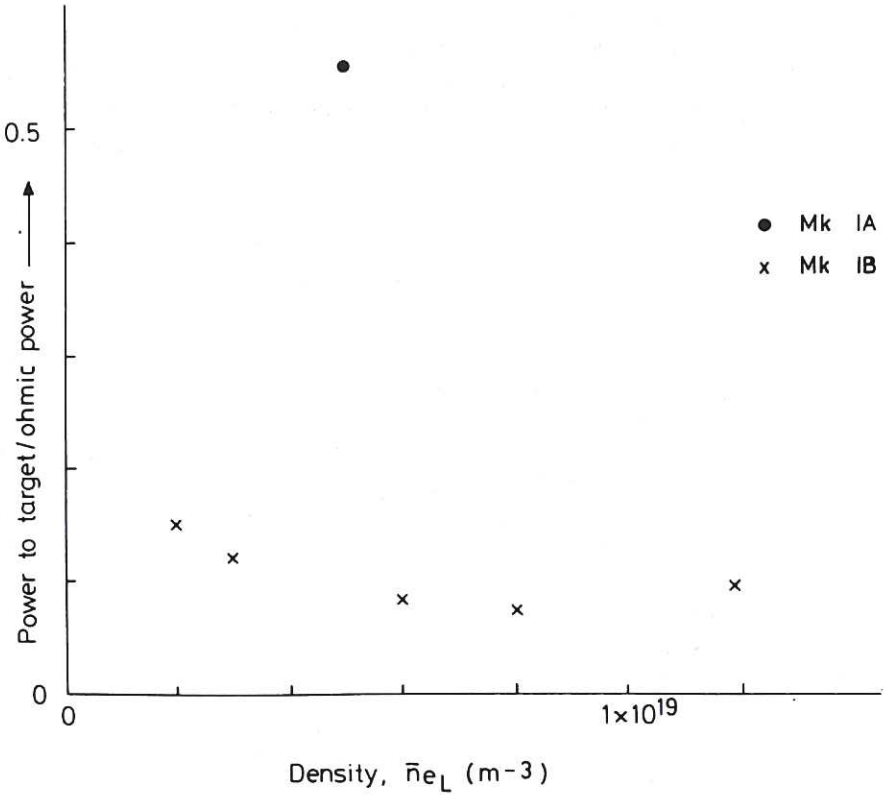

Fig.18 The fraction of ohmic power deposited on the target plate as a function of density, $\bar{n}_{eL}$ (MkIB).

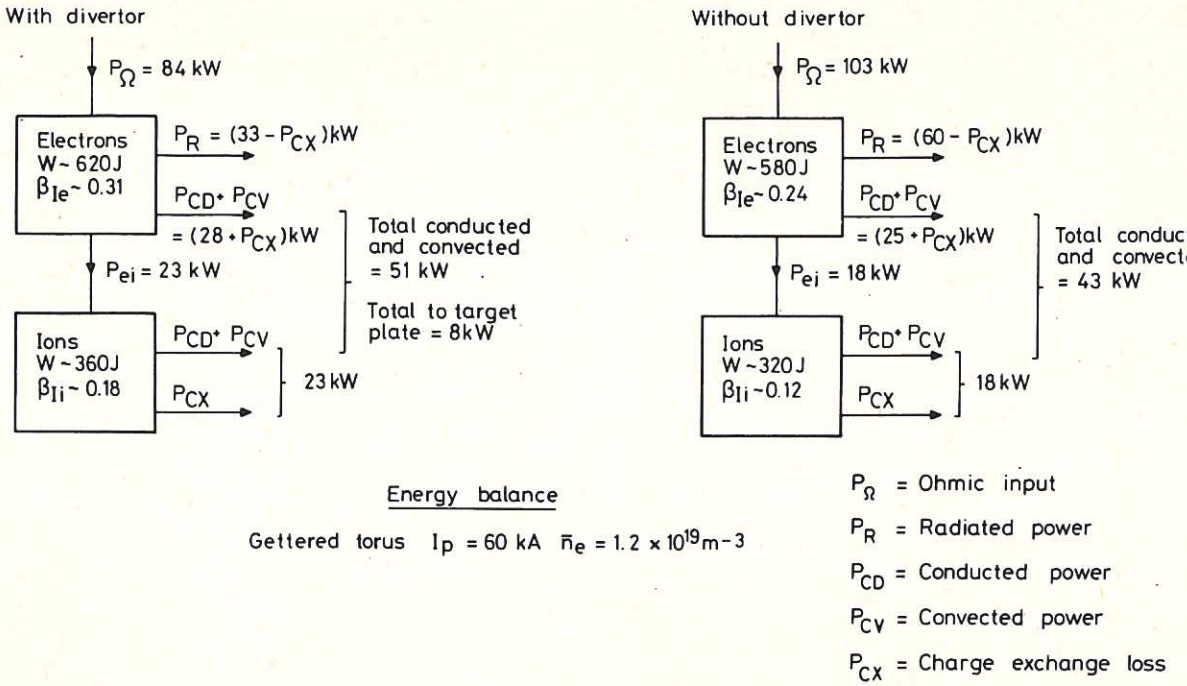

Fig.19 The overall energy balance, with and without divertor (SN as Figure 12, MkIB, $\bar{n}_{eL} = 1.2 \times 10^{19}$ m^{-3}).

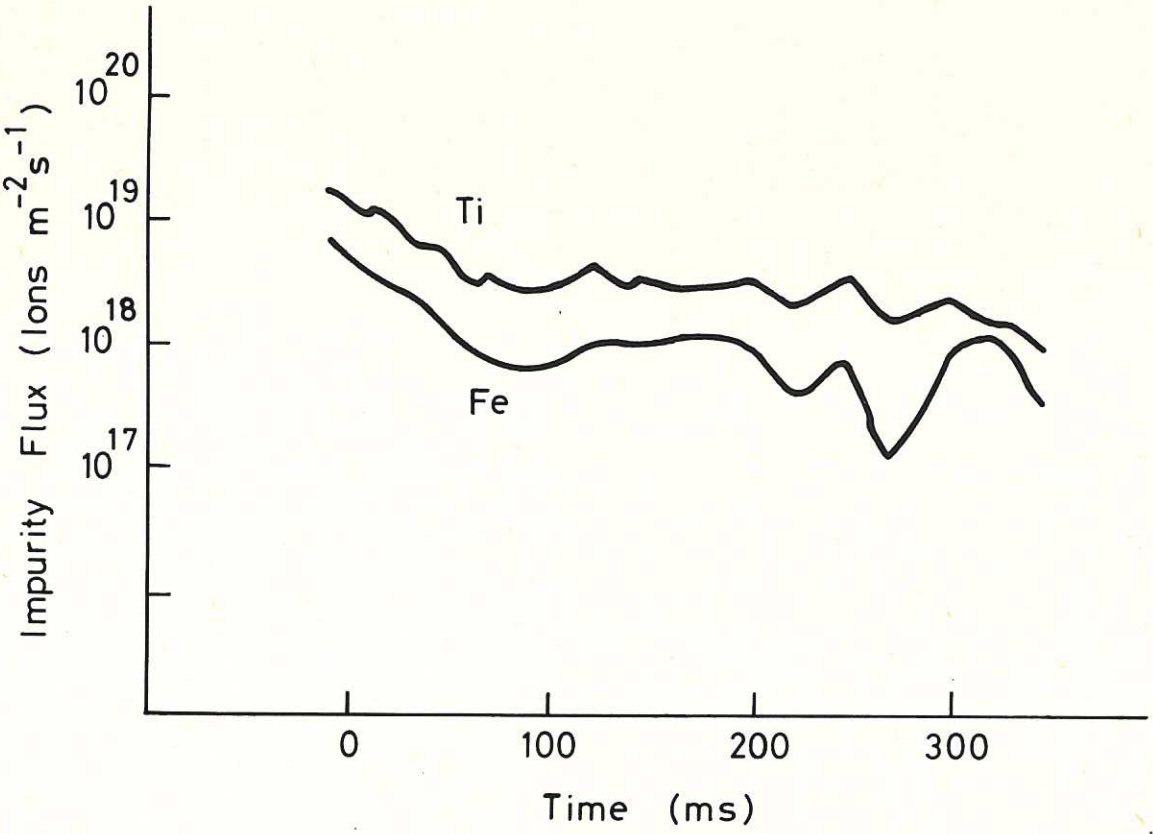

Fig.20 Fluxes of iron and titanium to a carbon collector probe positioned at r = 0.24m in a diverted discharge. (MkIB, $\bar{n}_{eL} \sim 6 \times 10^{18}$ m^{-3}).

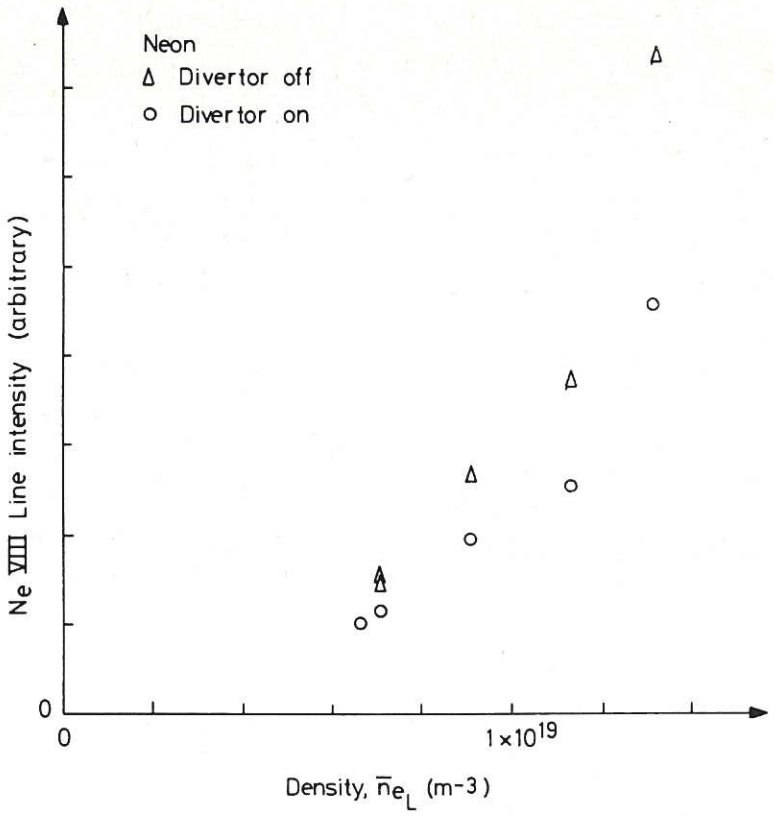

Fig.21 Neon line intensity, NeVIII, as a function of density $\bar{n}_{eL}$, with and without divertor, during neon puffing experiments (from 17/1/80, MkIB).

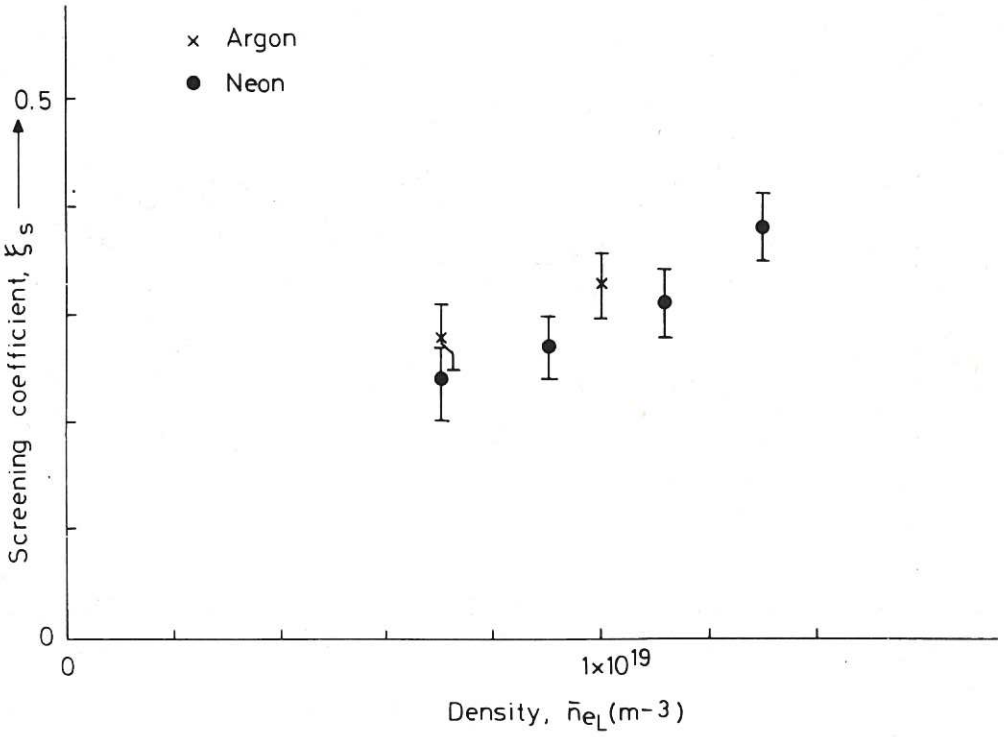

Fig.22 The shielding, or screening,, coefficient ξ_s as a function of density, $\bar{n}_{eL}$, from impurity gas puffing experiments (from 1/80, MkB).

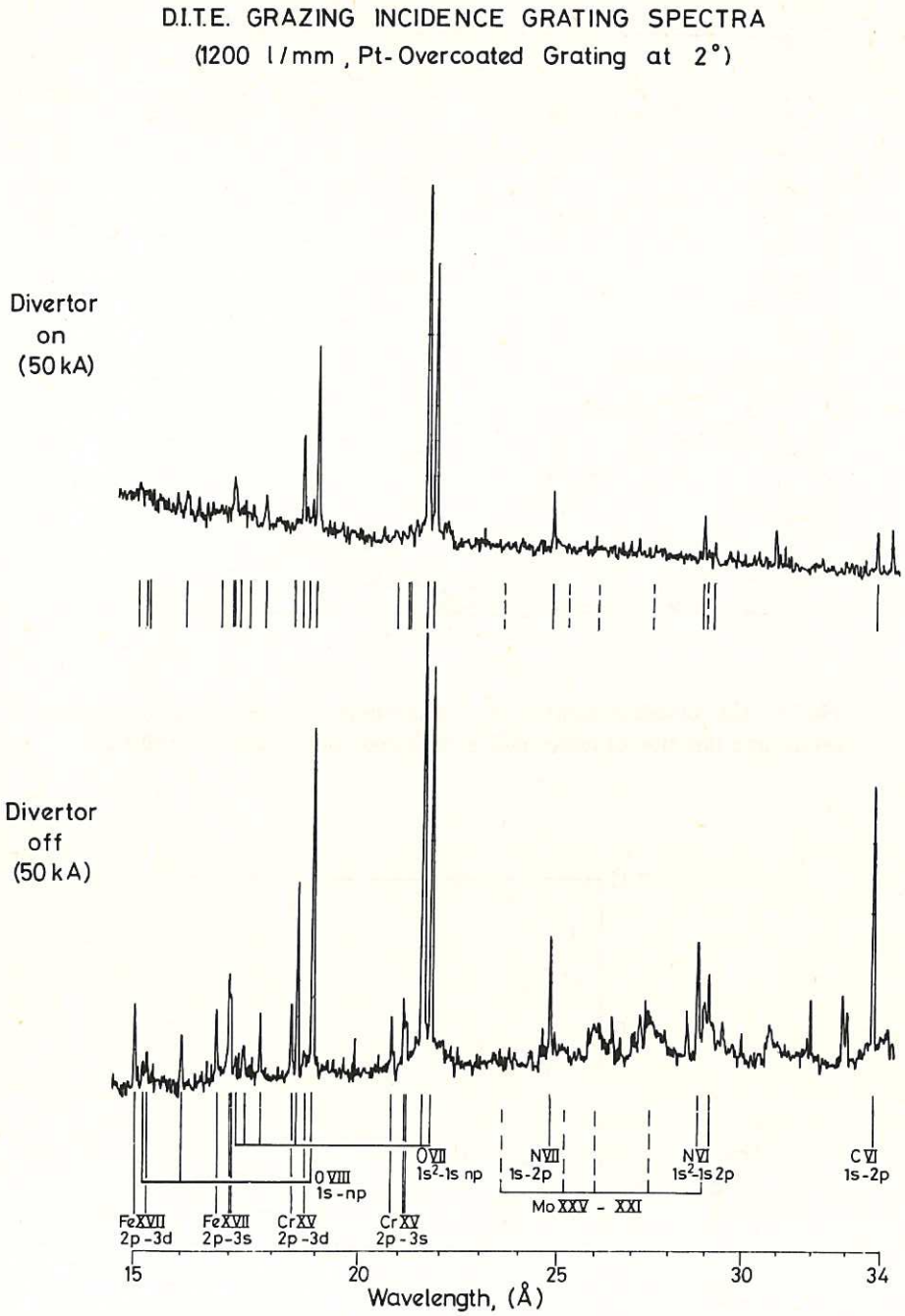

Fig.23 Grazing incidence spectra, obtained with and without divertor (MkIA).

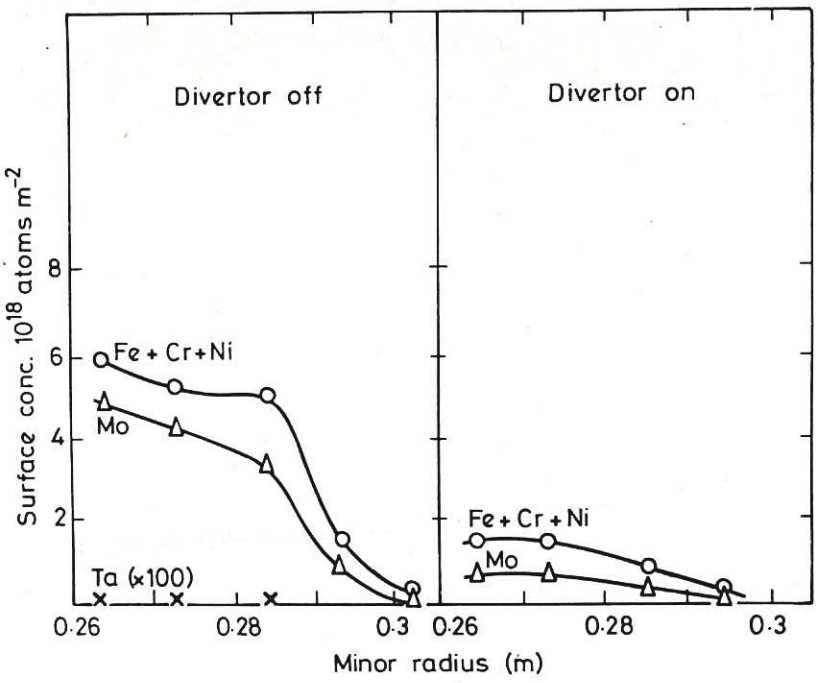

Fig.24 The surface concentration of metal impurities deposited on a carbon probe, as a function of minor radius, with and without divertor (MkIA).

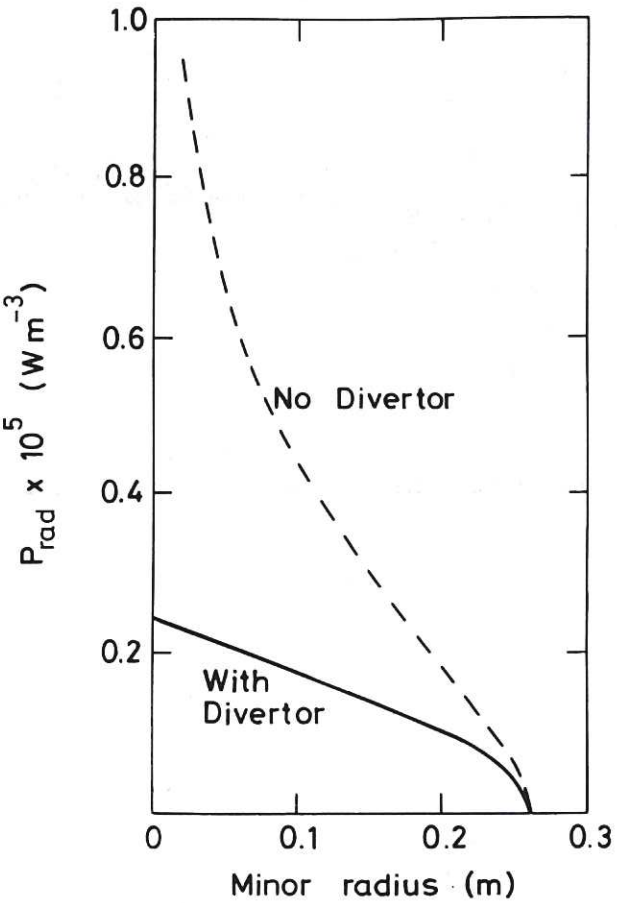

Fig.25 Profiles of radiated power, with and without the divertor (MkIA).

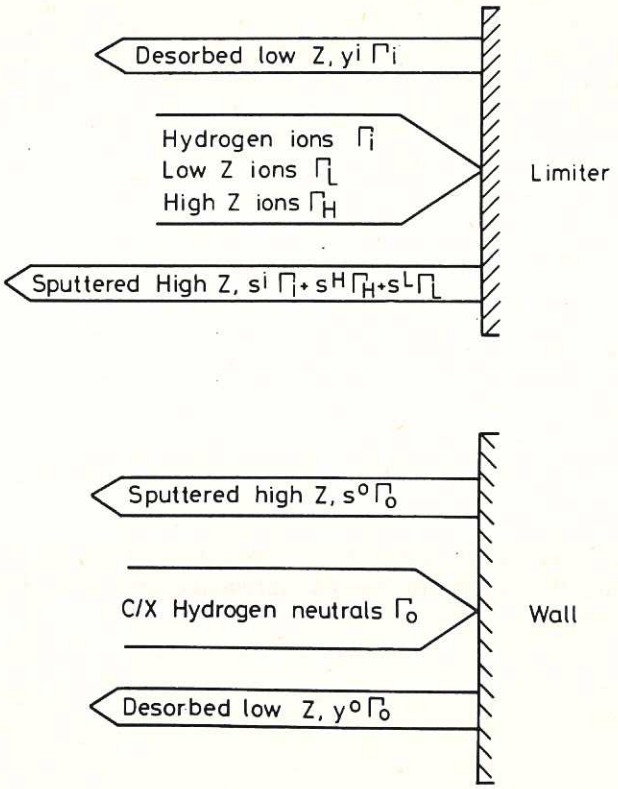

Fig.26 Diagramatic representation of the processes considered for impurity sources in the global model of impurity production.

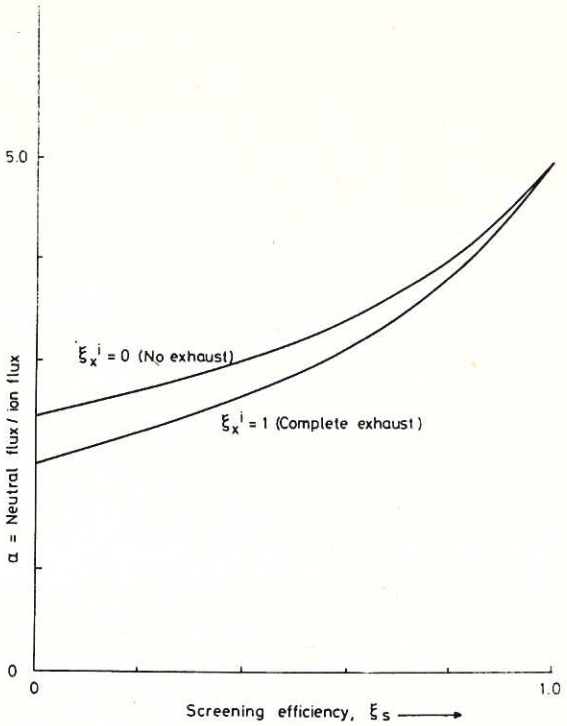

Fig.27 The ratio of the charge exchange radial flux to the wall, to ion flux to the limiters (divertor off) as a function of the working gas screening efficiency, ξ_s, for extremes of exhaust efficiency (ξ_x = 0 and 1).

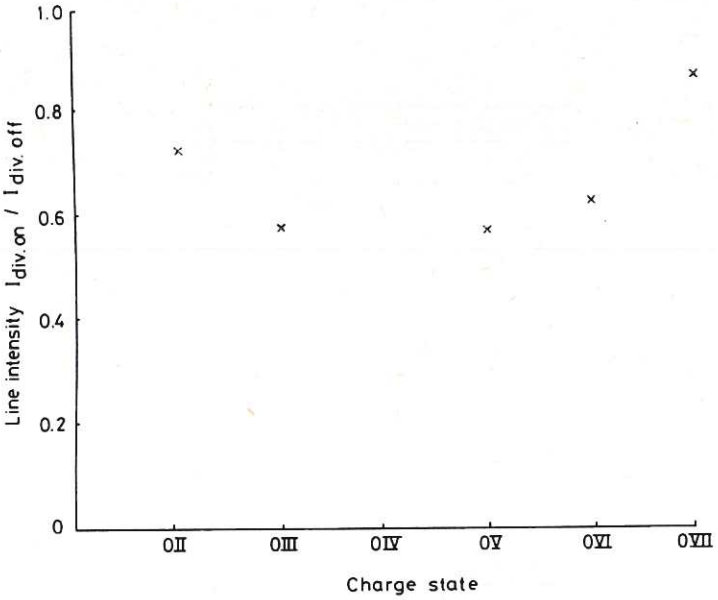

Fig.28 Line intensity ratios from oxygen impurity, divertor on to divertor off. Results are shown for different charge states, (from 9/79, MkIB, $\bar{n}_{eL} \sim 8 \times 10^{18}\ m^{-3}$).

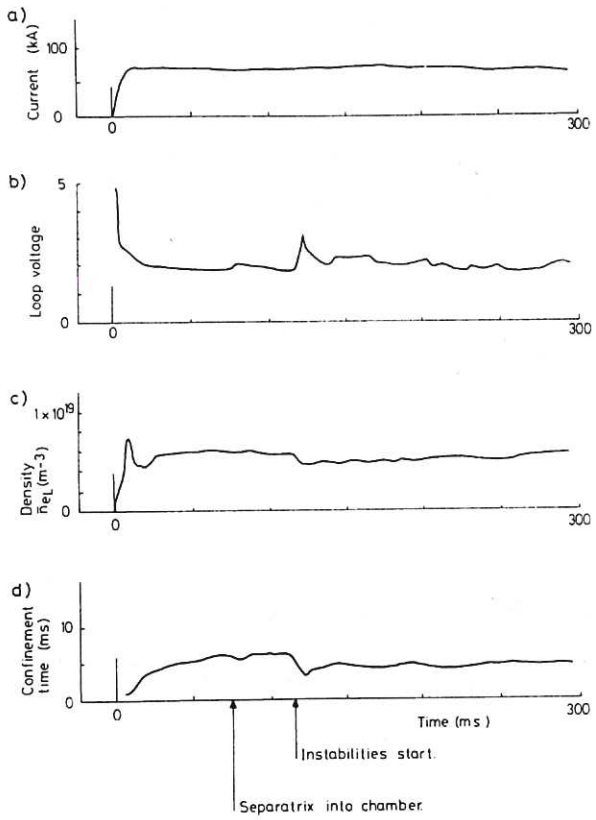

Fig.29 Characteristic results obtained during an unstable plasma (a) plasma current, (b) volts per turn, (c) average density $\bar{n}_{eL}$, (d) overall energy confinement time. The divertor was switched in mid-pulse (MkIB, SN 912011).

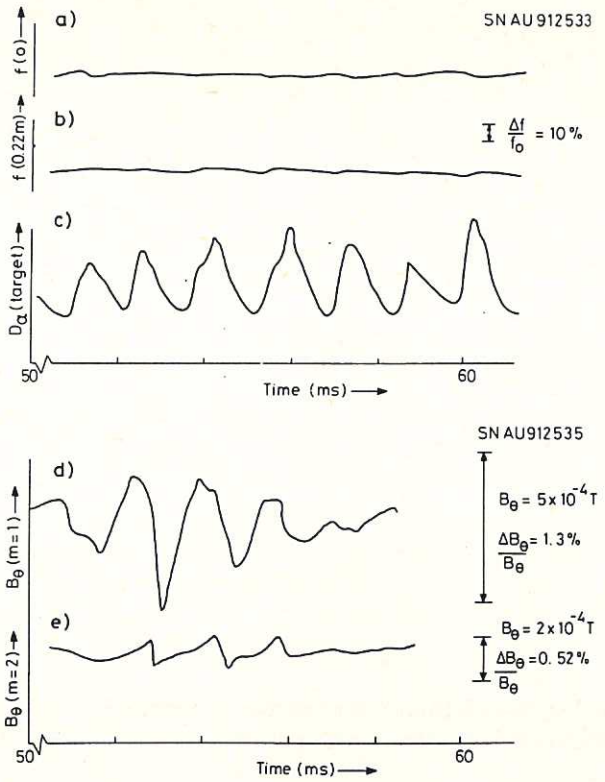

Fig.30 Details of parametric behaviour during the unstable period (with divertor).

(a) microwave interferometer signal f(o), through a chord at r = 0 (SN 912533)

(b) microwave interferometer signal f(0.22) through a chord at r = 22cm (SN 912533)

(c) the D_α signal from the target (SN 912533)

(d) the m = 1 component of the poloidal field (SN 912535)

(e) the m = 2 component of the poloidal field (SN 912535)

(MkIB, $\bar{n}_{eL} \sim 6 \times 10^{18}$ m^{-3}).

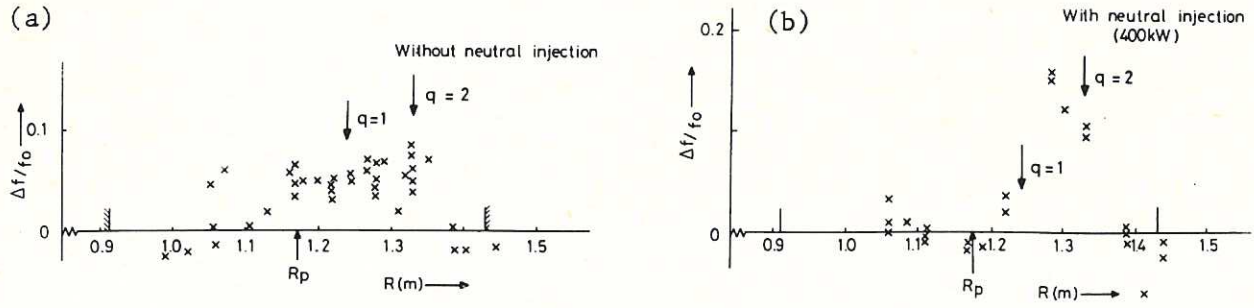

Fig.31 The spatial variation of the sawtooth perturbation to the microwave interferometer signal, Δf, during the unstable period (with divertor).

(a) with neutral injection (from 7/9/79)

(b) with 400kW of neutral injection (from 7/9/79)

Values are normalised to the signal f(o) through a chord at r = 0.

(MkIB, $\bar{n}_{eL} \sim 6 \times 10^{18}$ m^{-3}).

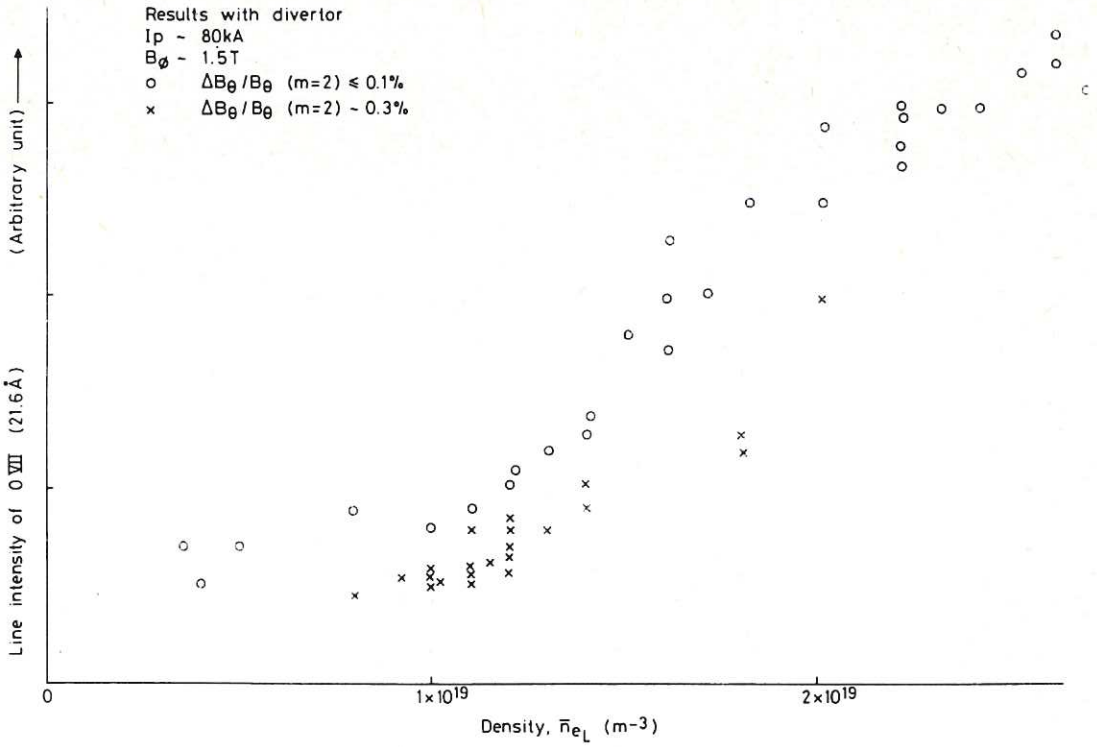

Fig.32 The intensity of the OVII line (2.16nm), as a function of density $\bar{n}_{eL}$. Results are shown for both stable and unstable discharges, in all cases with divertor (MkIB, not gettered, from 20/5/80).

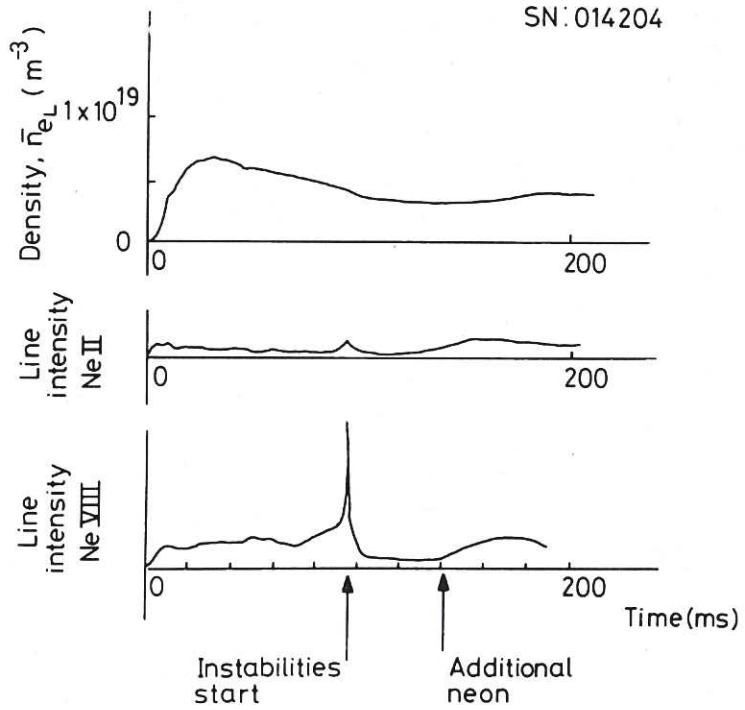

Fig.33 The effect of the unstable period on the NeII and NeVIII lines, with the divertor on.
(a) the average density $\bar{n}_{eL}$
(b) the NeII line intensity
(c) the NeVIII line intensity
Additional neon was introduced at 140ms (MkIB, SN 014204).

HER MAJESTY'S STATIONERY OFFICE

Government Bookshops

49 High Holborn, London WC1V 6HB
(London post orders: PO Box 569, London SC1 9NH)
13a Castle Street, Edinburgh EH2 3AR
41 The Hayes, Cardiff CF1 1JW
Brazennose Street, Manchester M60 8AS
Southey House, Wine Street, Bristol BS1 2BQ
258 Broad Street, Birmingham B1 2HE
80 Chichester Street, Belfast BT1 4JY

Publications may also be ordered through any bookseller